Analysis of Integrated Differential Absorption Radar and Subterahertz Satellite Communications Beyond 6G

Sergi Aliaga, Marco Lanzetti, *Graduate Student Member, IEEE*, Vitaly Petrov, Anna Vizziello, *Senior Member, IEEE*, Paolo Gamba, *Fellow, IEEE*, and Josep M. Jornet, *Fellow, IEEE*

Abstract—The integration of sub-Terahertz (sub-THz) communication beyond 100 GHz with differential absorption radar (DAR) as part of the evolution toward 5G-sdvanced and 6G nonterrestrial networks (NTNs) and beyond is critical for enabling intrinsic coexistence between these technologies. This study presents the first comprehensive analysis of an integrated sensing and communication (ISAC) system that combines satellite-centric sub-THz communications with DAR. We propose adapting the DAR waveform to be compatible with communication modulation, mathematically proving that this integration does not compromise DAR's sensing capabilities. In addition, we explore two methods to increase communication throughput with minimal impact on sensing performance: increasing the modulation order and increasing the number of symbols per chirp pulse. The results, validated through extensive simulations using published atmospheric models from the International Telecommunication Union (ITU) and the high resolution transmission molecular absorption database, reveal significant system tradeoffs. Our findings demonstrate that data rates can be enhanced up to 500 times without substantial degradation in estimation accuracy. However, excessively high data rates lead to significant estimation errors in the sensing system. This research underscores the potential of sub-THz ISAC systems for advanced satellite communications and remote sensing applications.

Index Terms—High frequency radar, meteorological radar, radar signal processing, satellite communications, terahertz communications.

I. INTRODUCTION

NTEGRATED Sensing and Communications (ISAC) represents a transformative approach in the convergence of

Received 23 June 2024; revised 27 August 2024; accepted 30 September 2024. Date of publication 14 October 2024; date of current version 29 October 2024. This work was presented at the IEEE WoWMoM'22 in Belfast, U.K., in June 2022 and received the Best Paper Award, available at https://ieeexplore.ieee.org/abstract/document/9842817 [DOI: 10.1109/WoWMoM54355.2022.00071]. This work was supported in part by the project FA9550-23-1-0254 by the U.S. Air Force Office of Scientific Research (AFOSR), and by the European Union under the Italian National Recovery and Resilience Plan (NRRP) of NextGenerationEU, partnership on "Telecommunications of the Future (PE00000001—program "RESTART")." (Corresponding author: Sergi Aliaga.)

Sergi Aliaga and Josep M. Jornet are with the Electrical Engineering and Computer Science Department, Northeastern University, Boston, MA 02115 USA (e-mail: aliaga.s@northeastern.edu).

Marco Lanzetti, Anna Vizziello, and Paolo Gamba are with the Electrical, Biomedical, and Computer Engineering Department, University of Pavia, 27100 Pavia, Italy.

Vitaly Petrov is with the Division of Communication Systems and Digital Futures, KTH Royal Institute of Technology, 11428 Stockholm, Sweden.

Digital Object Identifier 10.1109/JSTARS.2024.3480816

remote sensing and communication technologies, poised to revolutionize both fields. Uniting radar sensing and communications in a single platform through hardware commonalities and dual-purpose waveform design can drastically reduce the cost of each individual service [2], [3]. Moreover, ISAC technologies are particularly relevant for satellite platforms, where size, weight, and power requirements are stringent due to the hostile space environment [4], [5].

The use of ISAC also addresses another fundamental engineering limitation on the way to high-rate broadband connectivity with satellites in the frequency bands above 100 GHz—spectrum sharing and coexistence with Earth exploration satellite services (EESS) users [6], [7]. Notably, the recent surge in satellite megaconstellations aimed at offering high-throughput space-based Internet has raised significant coexistence concerns among the remote sensing community, primarily due to their operation at increasingly higher frequencies [8], [9]. Specifically, transmissions over wide bands in the millimeterwave (mmWave, \approx 30 GHz–100 GHz, including the Ka band [10]), sub-THz (100 GHz–300 GHz [11]), and even terahertz (THz, 300 GHz–3 THz) portions of the spectrum are anticipated [12], [13].

Moreover, these beyond-100 GHz frequencies are also envisioned for the next generation of wireless communication systems (6G) [14], [15], [16]. Large, yet underutilized, portions of the spectrum fall within this range, holding the key to multiple Gigabit-per-second (Gbps), or even Terabit-per-second (Tbps), data transfer speeds through multi-GHz bandwidths [17]. Transmission over such high frequencies is enabled by the latest advancements in electronic and photonic technologies [18], [19]. A clear example is the multiplier technology based on on-chip power combining, patented by NASA's Jet Propulsion Laboratory [20] and utilized in state-of-the-art THz communication platforms, such as the TeraNova platform at Northeastern University [21]. These advancements have supported successful demonstrations of multi-kilometer-long THz links [22] and project link closure even in satellite-to-airplane scenarios [23].

A common misconception, however, is that the prospective use of sub-THz bands above 100 GHz for communication immediately unlocks continuous frequency bands of tens to hundreds of GHz without interfering with existing 5G grade networks. However, the reality is that the existing spectrum regulations above 100 GHz are already scarce from the communication

perspective, offering only a few continuous bands wider than 10 GHz [24]. For example, the largest continuous band allocated for fixed and mobile communications between 100 and 200 GHz is only 12.5 GHz, which is less than the 14 GHz available between 57 and 71 GHz. To expand these bands, the coexistence of communications and sensing becomes critical, with ISAC technologies offering one of the most efficient solutions. Designing a waveform that serves both purposes, allowing the data exchange in certain subbands without compromising the accuracy of the coallocated sensing systems, is a tempting approach. In addition, such a design would still support the promise of ubiquitous broadband Internet coverage, while further justifying the substantial investment required for deploying these massive satellite systems [25], [26], [27].

A. Related Work

The idea of maximizing the mutually exclusive use of spectrum resources by efficiently combining wireless communications with radar sensing can be traced back many years [28]. Comprehensive overviews of the extensive literature on ISAC technologies, reported under various names such as Radar-Communications (RadCom), Joint Radar and Communication (JRC), Joint Sensing and Communication (JSC), ISAC, and others, can be found in [2], [3], [29], [30], [31], [32] (among many others). Below, we specifically aim to provide a brief overview of the most recent trends spearheading ISAC development in active remote sensing, which have motivated the development of the system evaluated in this article.

Anticipating the reach of 6G-grade performance levels, recent ISAC development trends have their roots in the use of increasingly powerful analog sources at higher frequencies. These new generation of sources enable link closure at orbital distances (> 100 km) [33], but are also raising coexistence concerns among remote sensing users above 100 GHz [24]. As history repeats itself, similar challenges were faced by researchers in wireless communications when exploring mmWave frequencies for 5G nonterrestrial networks (NTNs) [34], which led to significant coexistence challenges with existing radar onboard satellites [35] and airplanes [36].

In this context, multiple works propose ISAC systems operating below 100 GHz and successfully demonstrate the compatibility of remote sensing platforms with wireless communication. A subset of these alternatives considers using existing satellite infrastructure to perform bistatic remote sensing. Blázquez-García et al. [37] suggested using novel low-Earth orbit (LEO) satellite constellations operating at 11.7 GHz to achieve submeter resolution of targets on the Earth's surface. Meanwhile, Neinavaie et al. [38] combined Orthogonal Frequency Division Multiplexing (OFDM) reference signals from Starlink satellites and 5G-NR base stations, centered below 11.325 GHz, to achieve positioning errors below 10 m for aerial and ground vehicles, and stationary receivers. Alternatively, the adaptation of OFDM communication waveforms to perform Synthetic Aperture Radar (SAR), a widely used technique in atmospheric remote sensing, is also investigated. Garmatyuk et al. [39] proposed an OFDM waveform centered at 7.5 GHz achieving submeter radar resolution with a bit error rate (BER) below 5%. In contrast, Herschfelt et al. [40] outlined a 10 GHz solution for airplanes flying at 10 km and 100 m/s. The promising results of these and other solutions at similar frequencies are motivating the standardization of ISAC technologies already as part of 5 G [41].

As electronic frequency up-conversion progresses well beyond 100 GHz, new remote sensing, and potentially ISAC, platforms are being developed. Examples include the frequency modulated continuous wave (FMCW) radar proposed by Muppala et al. [42], achieving 6 dBm of transmit power at 223 GHz, or the vapor in-cloud profiling radar (VIPR) platform proposed by Cooper et al. [43], capable of 23 dBm of transmit power at 167 GHz. While both platforms operate with linear chirp waveforms (FMCW radars), the former has been utilized to achieve high-resolution target detection and ranging, with up to 0.3° azimuthal resolution at 60 m or more, and the latter is currently being used for in-cloud humidity profiling in the atmosphere, achieving less than 2 g/m³ bias over 84% of the time. With the rapid progression of these advanced remote sensing systems, multiple works propose efficient ISAC solutions at such frequencies, primarily targeting the object detection use case. Examples include the linear frequency modulation (LFM)-QAM waveform by Lyu et al. [44], achieving 2.5 mm resolution at 25 cm, or the correlation-based prototype proposed by Liu et al. [45], achieving sub-cm resolution at 60 cm. However, the development of ISAC solutions for the weather sensing use case beyond 100 GHz is undeservedly forgotten.

Specifically, before revolutionizing THz-band communications experimental research, one of the initial purposes of high-frequency analog multiplier technology was to perform weather sensing through differential absorption radar (DAR), an innovative remote sensing technique used at frequencies beyond 100 GHz [46]. Differential Absorption Radar (DAR), the focus of the analyzed ISAC system, is a signal processing technique that utilizes backscattered echo signals captured by FMCW radar platforms to estimate in-cloud water vapor density remotely. Specifically, the first implementation of DAR was initially proposed for the 173-193 GHz frequency range by Cooper et al. in [47]. A detailed description of the principles of operation of DAR is provided in Section II-B. Reciprocal to Differential Absorption LIDAR (DIAL), DAR targets the strong water absorption line located at 183 GHz, with multiple works documenting the initial attempts and early development within this specific band [48], [49], [50]. Cooper et al. presented the first experimental measurements from the ground in [43].

Furthermore, the first airborne measurements captured with the aforementioned VIPR platform were processed using DAR to estimate the in-cloud humidity, with results reported by Roy et al. in [51]. Authors emphasized the benefits of DAR when operated from airborne and space-borne platforms due to the reduced gaseous content near the radar platform, compared to ground-based operation. Consequently, Roy et al. simulated DAR from a LEO satellite at 400 km of altitude in [52], highlighting the design constraints when operating at frequencies between

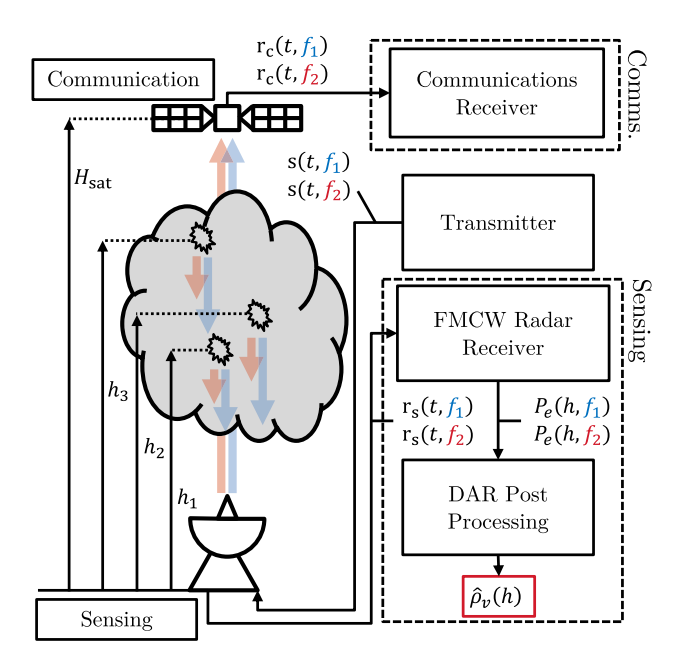


Fig. 1. Sub-THz DAR-ISAC system model, alternating between frequencies f_1 and f_2 for remote in-cloud sensing.

155.5 and 174.8 GHz, while avoiding the 174.8–191.8 GHz band reserved for passive EESS [53].

B. Novelty and Contributions

Despite the great imaging capabilities of DAR in the frequency bands above 100 GHz, the feasibility of its integration with a sub-THz communication system and the associated performance tradeoffs have not been comprehensively evaluated yet. By expanding our preliminary work [1], we aim to close this gap in the present article. To the best of the authors' knowledge, this is one of the first studies on the performance levels of an ISAC system involving satellite-centric sub-THz communications and DAR.

The main contributions of this study are thus summarized as

- Novel DAR Waveform: Adaptation of the proposed DAR-ISAC waveform to encompass larger data rates while still providing accurate sensing capabilities;
- Comprehensive Evaluation Methodology: A detailed theoretical and simulation framework to analyze the performance boundaries of the presented joint communication and DAR sensing system;
- An Extensive Numerical Study: In-depth simulation study demonstrating the presented concept and analyzing the performance tradeoffs between sensing accuracy and communications performance.

The rest of the article is organized as follows. Section II-A introduces the system model for the study and the joint DAR-ISAC waveform design. Then, the evaluation methodology, including communication and sensing performance, and channel simulation, is given in Section III. Later, Section IV presents the main numerical results. Finally, the key observations are discussed in Section V, while the main conclusions are summarized in Section VI.

TABLE I NOTATION USED IN THE ISAC SYSTEM ANALYSIS

Notation	Description		
	Input parameters		
f_1, f_2	Offline and Online frequencies		
$T_{ m c},T_{ m s}$	Chirp period and Symbol period		
B_{c}	Chirp bandwidth		
a	Chirp slope		
$N_{ m c}$	Number chirp pulses in $s(t, f_i)$		
$N_{ m sc}$	Number of symbols per chirp		
M	Modulation order		
γ	Roll-off factor		
	System Variables		
$s(t, f_i)$	Transmit signal		
$s_{\text{FMCW}}(t, f_i)$	Transmit sensing-only signal		
$\mathbf{r}_{\mathrm{s}}(t,f_{i})$	Backscattered received signal		
$\mathbf{r_c}(t, f_i)$	Satellite received signal		
$\eta_{\mathrm{s}}(t,f, ho_v(h))$	Sensing CIR		
$\eta_{\rm c}(t,f,\rho_v(h))$	Communications CIR		
A(t)	Baseband symbol sequence		
$\psi_{ m s}(au)$	Autocorrelation function of the transmitted signal		
f_b	Beat frequency		
h , Δh	Altitude range and altitude range resolution		
H_{sat}	Satellite altitude		
α	Backscattered echo amplitude		
au	Backscattered echo delay		
$\kappa(f,h, ho_v)$	Atmospheric absorption coefficient		
$P_e(h, f_i)$	Power-range profile		
$\rho_v(h)$	Water vapor density profile		
$\hat{\rho}_v(h)$	Estimated water vapor density profile		
	Radio and propagation parameters		
P_{Tx}	Transmit power		
$G_{\mathrm{Tx}},G_{\mathrm{Rx}},G_{\mathrm{sat}}$	Transmit, receive, and satellite antenna gain		
$L_{\rm spr}, L_{\rm abs}$	Spreading and absorption losses		
$N_{0,GS}, N_{0,sat}$	GS and satellite noise Power Spectral Density (PSD)		
	Performance metrics		
$E_{\rm b}/N_0$	SNR per bit		
$R_{\rm s},R_{b},R_{\rm t}$	Symbol rate, bit rate, and throughput		

II. SYSTEM MODEL AND WAVEFORM

In this section, we present the foundational framework of our proposed system by outlining the key components and interactions that define its operation. We begin by describing the system model, providing a comprehensive representation of the architecture and functional elements. Following this, we delve into the operational principle of the waveform enabling the proposed DAR-ISAC capabilities by describing in detail each of the system model's building blocks.

A. System Model

First, the main assumptions for our model are introduced. Fig. 1 schematically depicts the scenario under consideration, while Table I summarizes the key notation. We assume a Ground Station (GS) transmitting the ISAC waveform $\mathbf{s}(t,f_i)$, alternating between carrier frequencies f_1 and f_2 for adequate DAR operation, as detailed in Section II-B. The transmit signals are reflected off the cloud-forming hydrometeors and the corresponding backscattered echoes, $\mathbf{r}_{\mathbf{s}}(t,f_i)$, are captured back at the GS, either in a mono-static or bi-static configuration. The FMCW Radar Receiver processes the obtained echoes to estimate the backscattered signal power at each altitude h. For simplicity, we assume that the GS is pointing in the azimuth direction, so the radar range directly corresponds to the altitude range h, although

the backscattered echoes would also be observable in the case of slant path operation [43].

The corresponding power-range profiles at each frequency $P_e(h,f_i)$, are then compared by the DAR postprocessing block to extract the water vapor density information as a function of altitude. At the other end, after traversing the cloud mass in the atmosphere, the ISAC signal is picked up by a satellite receiver orbiting at an altitude $H_{\rm sat}$. The corresponding attenuated and noisy received signal ${\bf r}_{\rm c}(t,f_i)$ is demodulated, and the communication bits are extracted at the communications receiver stage. It is important to highlight that this configuration is agnostic of the link direction and could be replicated in a downlink setup, where the DAR sensing tasks are performed onboard the satellite, and the communication bits are demodulated at the GS.

B. DAR ISAC Waveform

Next, we provide an in-depth description of the principles of operation of our DAR-ISAC system, separating the different signal processing tasks by the blocks depicted in Fig. 1.

1) Transmit Waveform: To maximize the limited power output available in its operational band (200 mW at 167–174.8 GHz), the measurements necessary for DAR are obtained with a FMCW radar operation due to the increased sensitivity and larger duty cycle of continuous wave radars, as opposed to a pulsated radar approach. In addition, continuous wave transmission is desired to avoid the interruption of communication by dead times waiting for backscattered echoes. Thus, the transmit signal consists of a linear chirp of bandwidth $B_{\rm c}$, period $T_{\rm c}$, and the corresponding slope, $a = B_{\rm c}/T_{\rm c}$, with baseband equivalent

$$\mathrm{s_{FMCW}}(t) = \exp \left[j2\pi \left(\frac{a}{2}t^2 - \frac{B_\mathrm{c}}{2}t \right) \right]. \tag{1}$$

As demonstrated in the following section, the modulation of $s_{FMCW}(t)$ with a constant phase along the chirp does not affect the FMCW radar amplitude detection principle, thus opening the possibility of modulating a communication symbol through this constant phase. This modulation is the principal enabler of an ISAC system for amplitude detection and ranging, enabling decent data rates in short-range operation given that the corresponding symbol rate $R_{\rm s}=1/T_{\rm c}$ can be large with the adequate choice of T_c . It is important to note that, for the proper operation of a FMCW radar system, it is assumed that the maximum echo delay expected, $\tau = 2h/c$, is much lower than the chirp period, $\tau_{\rm max} \ll T_{\rm c}$, where c is the speed of light [54]. It is expected that for atmospheric remote sensing from the ground, echoes of the transmitted signal can originate at radar ranges beyond 10 km (around $70^{\circ} \mu s$ of round trip time), thus limiting the symbol rate through the choice of an adequate T_c as $R_s \ll 15$ kbaud. This effectively imposes a stringent limitation on the communication performance of the ISAC system.

To avoid these shortcomings and increase the data rate beyond the limits imposed by the choice of T_c , we modulate multiple communication symbols along the chirp period as

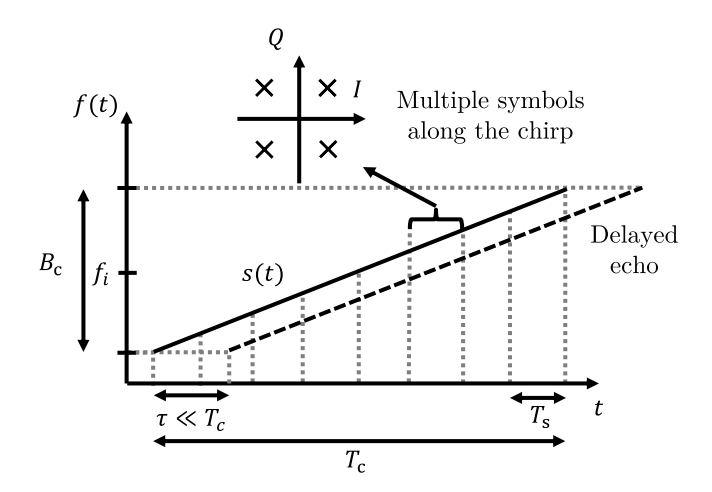


Fig. 2. Frequency-time plot of the ISAC signal compatible with DAR opera-

 $s(t) = A(t)s_{FMCW}(t)$, where

$$A(t) = \sum_{n=1}^{N_{sc}} (I_n + jQ_n)g(t - nT_s)$$
 (2)

corresponds to the transmitted baseband symbol sequence, $N_{\rm sc}$ is the number of symbols per chirp, $T_s=T_{\rm c}/N_{\rm sc}$ is the corresponding symbol period, I_n and Q_n are the in-phase and quadrature components of the symbol, respectively, and g(t) is the unit-energy pulse shaping the symbols transmitted. Fig. 2 schematically depicts the transmitted signal centered at the carrier frequency f_i in a frequency-time plot.

2) FMCW Radar Receiver: At the input of the FMCW Radar Receiver block, the received echo signal $r_s(t, f_i)$, consists of the multiple attenuated and noisy copies of s(t) as

$$\mathbf{r}_{\mathbf{s}}(t, f_i) = \sum_{j} \alpha(\tau_j, f_i) \mathbf{s}(t - \tau_j) + w(t)$$
 (3)

where $\alpha(\tau_i, f_i)$ is the backscattered echo amplitude resulting from the round trip to the altitude $h_j = c\tau_j/2$ at the frequency f_i , and w(t) is the corresponding baseband additive white Gaussian noise (AWGN). As discussed in the following section, the choice of the two frequencies f_1, f_2 , is made so the frequency dependence in the attenuation of the signal is primarily due to the difference in the absorption between the two frequencies. The main task of the radar receiver is then to estimate the backscattered signal power at each frequency as a function of range altitude through the estimation of $\alpha(\tau_i, f_i)$, given that $P_e(h, f_i) = \alpha(\tau, f_i)^2$. As detailed in Section III-C, given the unitary amplitude of s(t), $\alpha(\tau_j, f_i)$ is assumed to capture the transmit power P_{Tx} , as well as the transmit antenna gain G_{Tx} , thus having units of power when squared. The estimator function of the signal amplitude based on generalized maximum likelihood (GML) estimation principles under Additive White Gaussian Noise (AWGN) is [55]

$$\hat{\alpha}_{\text{GML}}(h) = \frac{\left| \int_{T_c} \mathbf{r}_{\mathbf{s}}(t) \mathbf{s}^*(t-\tau) dt \right|}{\int_{T_c} \left| \mathbf{s}(t-\tau) \right|^2} \tag{4}$$

where the dependence with h is captured through the dependence with the delay τ , and the dependence with frequency has been omitted for clarity. From here, we separate the estimation in three distinct cases:

1) Sensing only (s(t) =
$$s_{FMCW}(t)$$
):

Here, the estimator expression is reduced to the well-known target amplitude estimation through beat frequency f_b as

$$\hat{\alpha}_{\text{GML}}(h) = \frac{1}{T_{\text{c}}} \left| \int_{T_{\text{c}}} \mathbf{r}_{\text{s}}(t) \mathbf{s}_{\text{FMCW}}^{*}(t) \exp\left[-j2\pi f_{b}t \right] dt \right|$$

$$= \frac{1}{T_{\text{c}}} \left| F\left[\mathbf{r}_{\text{s}}(t) \mathbf{s}_{\text{FMCW}}^{*}(t) \right] \right| \tag{5}$$

where $f_b=-a\tau=-\frac{B_c}{T_c}\frac{2h}{c}$, and $F[\cdot]$ indicates the Fourier Transform operator.

2) One Symbol Per Chirp ($N_{sc} = 1$):

When a single symbol is modulated, the transmitted signal becomes $\mathbf{s}(t) = |A| \exp[j\varphi] \mathbf{s}_{\mathrm{FMCW}}(t)$, assigning a constant phase, $\varphi = \arctan(Q/I)$, and amplitude, $|A| = \sqrt{I^2 + Q^2}$, to the entire chirp pulse (the pulse g(t) is omitted for clarity). In this case, amplitude estimation can also be performed through beat frequency, only requiring compensation for the symbol amplitude as

$$\hat{\alpha}_{\text{GML}}(h) = \frac{1}{|A|T_c} \left| F\left[\mathbf{r}_{\mathbf{s}}(t) \mathbf{s}_{\text{FMCW}}^*(t) \right] \right|. \tag{6}$$

Thus, the power-range profile estimation when only a single symbol is modulating every chirp ($N_{\rm sc}=1$) is identical to that of the unmodulated FMCW signal. In other words, when the transmitted signal s(t) is modulated with $N_{\rm sc}=1$ symbols per chirp, the power-range profiles estimated and used as input to the DAR postprocessing stage, $P_e(h,f_i) \ \forall i \in [1,2]$, are identical to those estimated when the transmitted signal is unmodulated and no ISAC capabilities are considered. For this reason, given that the DAR postprocessing stage is making the humidity estimation based on *identical echo observations*, we can conclude that the DAR humidity estimation performance is not compromised by communication when $N_{\rm sc}=1$. This important observation is further explored in Section IV-A

3) Increasing the Data Rate ($N_{\rm sc} > 1$):

When considering the modulation of the chirp pulse with the symbol sequence A(t) the transmitted signal becomes $\mathbf{s}(t) = A(t)\mathbf{s}_{\text{FMCW}}(t)$, and the Generalized Maximum Likelihood (GML) estimator reduces to

$$\hat{\alpha}_{\text{GML}}(h) = \frac{\left| \int_{T_c} \mathbf{r_s}(t) A^*(t-\tau) \mathbf{s}_{\text{FMCW}}^*(t) \exp\left[-j2\pi f_b t \right] dt \right|}{\int_{T_c} \left| A(t-\tau) \right|^2 dt}$$

for which the implementation through beat frequency estimation is no longer possible due to the dependence of the symbol sequence on the delay τ . In this case, $\hat{\alpha}_{\text{GML}}(h)$ becomes a correlation-based estimator, depending on the autocorrelation properties of the transmitted signal, $\psi_s(\tau) = E\{s(t)s^*(t-\tau)\}$, whose narrow shape is not guaranteed due to the random nature of the transmitted signal sequence.

Delay consideration: Despite the potential limitation outlined above, if we assume that the delay is much smaller than the

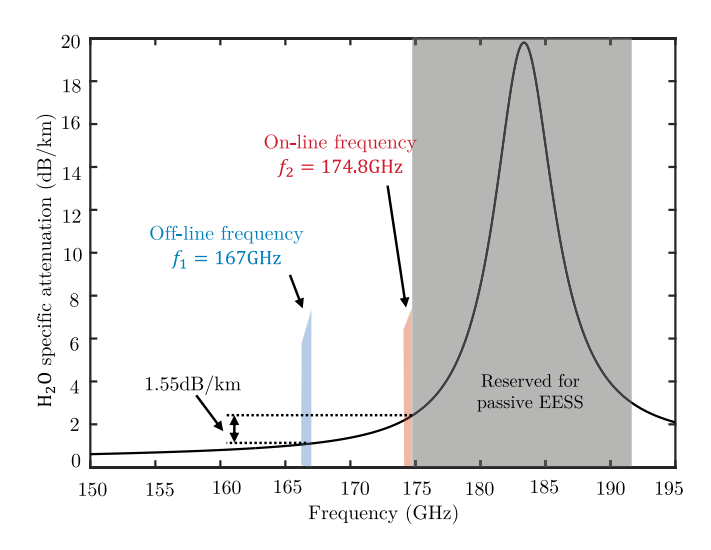


Fig. 3. Water vapor specific attenuation at sea level calculated using the ITU Recommendation ITU-R P.676-12 [56] and Recommendation ITU-R P.835 [57].

symbol time $\tau \ll T_s$, we can approximate $A(t-\tau) \approx A(t)$, making the estimation still well approximated through the beat frequency:

$$\hat{\alpha}_{\text{GML}}(h) = \frac{|F\left[\mathbf{r}_{\text{s}}(t)\mathbf{s}^{*}(t)\right]|}{\int_{T_{c}}|A(t)|^{2}dt}.$$
(8)

This assumption only holds when T_s is large compared to τ , i.e., when

$$N_{\rm sc} \ll cT_{\rm c}/(2h). \tag{9}$$

Therefore, for low values of $N_{\rm sc}$, a tradeoff between DAR operation and communication arises, where the estimation error increases as the data rate is increased through the choice of larger $N_{\rm sc}$. In light of this, it would seem preferable to choose longer chirps, in favor of larger values of $N_{\rm sc}$. However, an upper bound on the choice of $T_{\rm c}$ arises from the coherence time of the observed scene, not allowing a choice of $T_{\rm c}$ arbitrarily large. Notably, none of these considerations seem to be affected by the modulation order M allowing for the transmission of complex modulations without affecting sensing, as long as the signal-to-noise ratio (SNR) requirements are met. These important observations are further explored in Section IV-B.

3) DAR Signal Postprocessing: The main operational principle of DAR involves comparing the backscattered power at two distinct frequencies. The water vapor content in the target range bin is then estimated from the difference in these two backscattered powers, assuming this difference is primarily due to the variation in water vapor absorption between the two frequencies. Fig. 3 schematically depicts the differential absorption principle through the selection of two frequencies: one as close as possible to an absorption peak, known as the online frequency (f_2) , and another with a much lower specific attenuation, known as the offline frequency (f_1) . The absorption lines of water vapor at these frequencies, where the wavelength is comparable to the

¹The specific attenuation is defined as the absorption loss calculated along 1 km with constant absorption coefficient.

size of cloud-forming hydrometeors, exhibit considerably wide profiles, spanning a relative bandwidth of 1–10%, compared to around 0.01% for DIAL. Implementing a system capable of transmitting two narrow-band signals at frequencies separated by a fractional bandwidth of 1–10% is extremely challenging and only recently became achievable thanks to the aforementioned frequency-multiplying analog technology.

To retrieve the humidity profile $\rho_v(h)$, from the estimated power-range profiles $P_e(h,f_i)$, we utilize the regularized least squares approach presented in [58], for which a brief explanation is provided in Appendix A for completeness, as well as the absorption models from the HIgh resolution TRANsmission molecular absorption (HITRAN) database.

Bandwidth consideration: One key assumption of DAR, with direct implications to an ISAC system based on it, is the assumption that the absorption losses along the chirp bandwidth are constant, which only holds for narrow chirp bandwidth values. For this reason, in addition to an upper bound limit on $B_{\rm c}$, the bandwidth of the symbol sequence transmitted also has to be narrower than $B_{\rm c}$. Assuming root-raised-cosine (RRC) pulse-shaping with roll-off γ , this translates to $R_{\rm s}(1+\gamma) < B_{\rm c}$, which can be further reduced to

$$N_{\rm sc} < B_{\rm c} T_{\rm c} / (1 + \gamma).$$
 (10)

As shown in Section IV, given the scale of the measured ranges, this limitation in $N_{\rm sc}$ is less stringent than the one in (9). It is also important to note that a large system bandwidth would also result in larger system noise at the receiver, thus limiting the range of the radar by reducing the SNR in reception.

4) Communications Receiver: The communications receiver on-board the satellite captures the transmitted signal and demodulates it to extract the corresponding information bits. The demodulation process at frequencies beyond 100 GHz, after carrier and symbol synchronization, is generally divided into two stages: 1) analog frequency down conversion to baseband or intermediate frequency for adequate sampling, and 2) sampling and symbol detection through matched filtering or correlation.

The analog frequency downconversion step in the demodulation process is necessary when operating beyond 100 GHz because both the received signal $r_c(t)$, and the carrier FMCW signal are high-frequency passband signals, which would require immensely high sampling rates for a passband software implementation of the matched filter (i.e., > 100 Gsps). To alleviate this requirement, the received signal is down-converted to an intermediate frequency and efficiently sampled. In general, current state-of-the-art sub-THz sources, e.g., [18], [19], [20], [21], [43] and others, operate thanks to the use of multiple heterodyning stages, where the carrier frequency of an initial synthesizer is multiplied several times. These types of architectures are often referred to as superheterodyne systems, and they can vary considerably even for the same targeted carrier frequency (e.g., number of multiplying stages, initial synthesizer frequencies, antenna type). Notably, these architectures are not unique, and multiple configurations could achieve adequate analog frequency downconversion.

After frequency downconversion and sampling, matched filtering of the baseband equivalent signal is matched to the initial

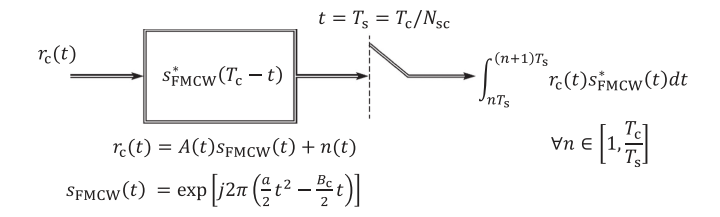


Fig. 4. Complex baseband matched filter for the proposed DAR-ISAC waveform.

baseband FMCW radar signal $s_{\rm FMCW}(t)$. The only difference between the matched filtering of the proposed DAR-ISAC system and conventional matched filtering would be the difference in the sampling time after the matched filter. Concretely, we note that, while $s_{\rm FMCW}(t)$ has a duration of $T_{\rm c}$, each symbol modulating it has a duration $T_{\rm s} = T_{\rm c}/N_{\rm sc}$, as indicated in Fig. 2. For this reason, although the receiver onboard the satellite is matched to $s_{\rm FMCW}(t)$, the sampling is carried out at intervals of duration $t = T_{\rm c}/N_{\rm sc}$. A schematic representation of this matched filter implementation is depicted in Fig. 4 for reference.

Eventually, after analog frequency down-conversion and detection through matched filtering, the transmitted symbols are converted into information bits, and error metrics are calculated, as described in Section III-B.

III. EVALUATION METHODOLOGY

In this section, we detail the evaluation methodology employed to assess the performance of the proposed DAR-ISAC system. First, we focus on the accuracy and reliability of the system's sensing capabilities. Next, we evaluate the system's ability to transmit and receive information efficiently and reliably. In both cases, we analyze the performance tradeoffs of utilizing the proposed DAR-ISAC system instead of a dedicated sensing or communication system utilizing the same resources. Finally, we describe the simulation of the atmospheric channel to examine the impact of various channel conditions on overall system performance.

A. Sensing

First, we evaluate the ISAC system's sensing performance by studying the estimation error on the retrieved humidity profiles. Concretely, we measure the mean absolute error (MAE) of the system as

$$MAE = E\{|\hat{\rho}_v - \rho_v|\} \tag{11}$$

where $\hat{\rho}_v$ is the estimated humidity, ρ_v is the true humidity, and $E\{\cdot\}$ indicates the expected value operator.

While the regularized least squares approach used is designed to minimize the mean squared error (MSE) when errors are normally distributed (see Appendix A), we choose to report the MAE instead of MSE. This decision aligns the performance results of our DAR-ISAC system with those of DAR-exclusive systems, such as those reported by Roy et al. [58], thus facilitating a more direct comparison. After evaluating both metrics, it is

found that the MSE results do not provide additional insights beyond those observable in the MAE results, so we decide to report only the latter for clarity. Moreover, the absolute error, or bias, offers several advantages over the MSE, such as maintaining the same units with the estimated metric (i.e., gm⁻³), providing a direct measure of systematic error—which is critical in sensing equipment-and being more robust to outliers.

In order to evaluate the sensing performance tradeoff between our DAR-ISAC system and a DAR-exclusive system, we choose to normalize the observed MAE by the MAE observed with the unmodulated DAR signal, MAE $_{DAR}$, and, thus, we define the MAE gain as

$$G_{\text{MAE}} = \frac{\text{MAE}_{\text{DAR}}}{\text{MAE}_{\text{ISAC}}} \tag{12}$$

where the MAE_{DAR} is identical to that of our DAR-ISAC system when $N_{\rm sc}=1$, as indicated in Section II-B.

B. Communication

Next, we evaluate the ISAC system's communication performance by comparing it to a conventional system that uses the entire chirp bandwidth $B_{\rm c}$, to modulate a carrier with a symbol stream. Concretely, the bit rate $R_{\rm b}$ of the proposed DAR-ISAC system, which is limited by the delay and bandwidth considerations outlined in Section II-B, is related to the system parameters as

$$R_{\text{b,ISAC}} = \frac{N_{\text{sc}}}{T_c} \log_2(M). \tag{13}$$

From this equation, we infer that the two ways to increase the data rate are by increasing the modulation order M or increasing the number of symbols per chirp $N_{\rm sc}$ as $N_{\rm sc}$ is directly related to the chirp time, $T_{\rm c}$, through (9) and (10). However, there is a tradeoff for each option: increasing the modulation order requires a higher SNR, and increasing $N_{\rm sc}$ results in a larger estimation error. These observations are further evaluated in Section IV

Conversely, utilizing the entire chirp bandwidth for modulating a carrier without sensing capabilities would yield the following bit rate:

$$R_{\text{b,Comms.}} = \frac{B_{\text{c}}}{(1+\gamma)} \log_2(M). \tag{14}$$

Fast communication is just as important as reliable communication. For this reason, we also analyze the SNR per bit $E_{\rm b}/N_{\rm 0}$, which is directly related to the system's BER. For the presented ISAC system, the SNR per bit becomes

$$\frac{E_{\rm b}}{N_{0\,\rm ISAC}} = \frac{B_{\rm c}T_{\rm c}}{\log_2(M)N_{\rm sc}} \text{SNR}_{\rm sat}$$
 (15)

where ${\rm SNR_{sat}} = P_{\rm Rx,sat}/P_{n,\rm sat}$ is the SNR at the satellite receiver, and the noise power is modeled through the system noise PSD $P_{n,\rm sat} = N_{0,\rm sat}B_{\rm c}$. The received power at the satellite $P_{\rm Rx,sat}$ is evaluated at the online frequency f_2 , since it has the largest loss, and is modeled through the Friis transmission equation as

$$P_{\text{Rx,sat}} = \frac{P_{\text{Tx}} G_{\text{Tx}} G_{\text{sat}}}{L_{\text{spr}}(f_2, H_{\text{sat}}) L_{\text{abs}}(f_2, H_{\text{sat}}, \rho_v(H_{\text{sat}}))}$$
(16)

where $P_{\rm Tx}$ and $G_{\rm Tx}$ are the transmit power and antenna gain, respectively, $G_{\rm sat}$ is the satellite antenna gain, $L_{\rm spr}=(4\pi hf/c)^2$ are the spreading losses, and $L_{\rm abs}(f,h,\rho_v)$ are the absorption losses for a given frequency, altitude, and humidity. Details about the modeling of the absorption losses are provided in Section III-C. From (15), we can observe the tradeoff between data rate and SNR again, since either of the two options of increasing R_b would result in a lower SNR per bit.

Again, the expression for the SNR per bit in a communicationonly system would differ, as a higher data rate results in less energy being allocated to each bit, thus resulting in

$$\frac{E_{\rm b}}{N_{0\,\rm Comms.}} = \frac{(1+\gamma)}{\log_2(M)} \text{SNR}_{\text{sat}}.$$
 (17)

To combine both metrics, $R_{\rm b}$ and $E_{\rm b}/N_{\rm 0}$, we analyze the total throughput of the proposed system $R_{\rm t}$, defined as the number of *correct* bits transmitted over time. Concretely, utilizing the previous derivations, the throughput of the proposed DAR-ISAC system and the equivalent communication-only throughput become, respectively:

$$R_{\text{t,ISAC}} = R_{\text{b,ISAC}} \left(1 - \text{BER}(E_{\text{b}}/N_{0,\text{ISAC}}, M) \right) \tag{18}$$

$$R_{\text{t.Comms.}} = R_{\text{b.Comms.}} (1 - \text{BER}(E_{\text{b}}/N_{0.\text{Comms.}}, M))$$
 (19)

where $BER(E_b/N_0, M)$ indicates the BER of an M-QAM system under AWGN. Based on these results, one might be inclined to think that there is no communications tradeoff in using the proposed ISAC system since the decrease in data rate might be compensated by the larger energy per bit. However, due to the nonlinear relation between the BER and the SNR per bit, if we normalize the ISAC throughput in (18) with the equivalent communication-only throughput in (19), we can indeed observe that such a tradeoff exists

$$\frac{R_{\text{t,ISAC}}}{R_{\text{t,Comms.}}} = \frac{N_{\text{sc}}(1+\gamma)}{B_{\text{c}}T_{\text{c}}} \frac{\left(1 - \text{BER}\left(\frac{B_{\text{c}}T_{\text{c}}}{\log_2(M)N_{\text{sc}}} \text{SNR}_{\text{sat}}, M\right)\right)}{\left(1 - \text{BER}\left(\frac{(1+\gamma)}{\log_2(M)} \text{SNR}_{\text{sat}}, M\right)\right)}.$$
(20)

Although the second term in (20) is greater than 1 due to the larger SNR per bit in our ISAC system, it is compensated by the first term, which is largely smaller than 1 for the system values considered. Thus, there exists a clear communications tradeoff in using the proposed DAR-ISAC system. This tradeoff is further evaluated in detail in Section IV-C.

C. Channel Simulation

In this section, we describe the simulation of the atmospheric channel, which is critical for evaluating the performance of the proposed DAR system integrated with Sub-THz-band communications. The simulation process involves modeling the channel impulse response (CIR) of the sensing and communication channels, $\eta_s(t, f, \rho_v(h))$ and $\eta_c(t, f, \rho_v(h))$, respectively, as well as adding the corresponding AWGN. Fig. 5 schematically depicts the simulation process. The humidity profile used as an input to the simulation, $\rho_v(h)$ is then used as the ground truth to measure the estimation error of our system.

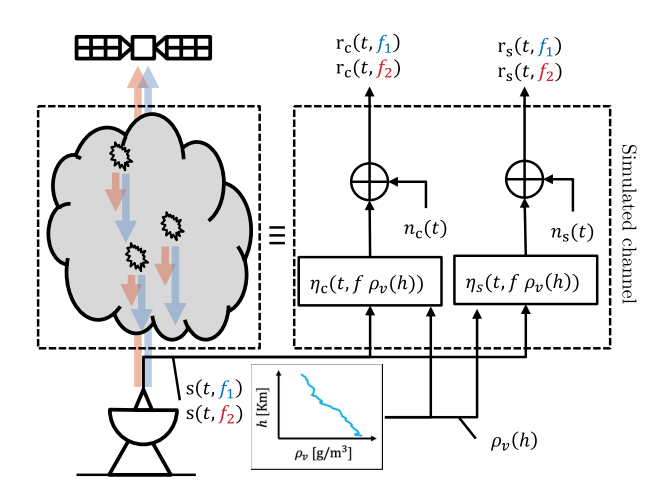


Fig. 5. Simulating the atmospheric channel given the assumed humidity profile $\rho_v(h)$, as an input.

1) Sensing CIR: For the CIR of the sensing channel, we consider signal reflections at every radar range bin, that is

$$\eta_{s}(t, f, \rho_{v}(h)) = \sum_{j=1}^{h_{\text{max}}/\Delta h} \alpha(f, 2j\Delta h, \rho_{v}(j\Delta h)) \delta(t - \tau(2j\Delta h))$$
(21)

where $\alpha(f,h,\rho_v)$ is the channel gain for a certain frequency f and altitude h, given a humidity ρ_v ; $\delta(t)$ is the Dirac Delta, and $\tau(h)=2h/c$ is the channel delay, accounting for the round trip time. For computational efficiency, while considering a realistic altitude range of backscattered reflections, the maximum altitude for which reflections are captured is set to $h_{\rm max}=10$ km. Moreover, we consider that there are no reflections in the first 100 m in front of the GS, or, equivalently, $\alpha(f,h,\rho_v(h))=0$ for h<100 m.

2) Communications CIR: For the CIR of the communication channel, given that $H_{\rm sat} \gg h_{\rm max}$, we only consider the line of sight (LoS) signal at the receiver, thus

$$\eta_{c}(t, f, \rho_{v}(h)) = \alpha(f, H_{\text{sat}}, \rho_{v}(H_{\text{sat}}))\delta(t - \tau(H_{\text{sat}})). \tag{22}$$

3) Channel Gain: Computed as follows:

$$\alpha(f, h, \rho_v) = \left(\frac{P_{\mathsf{Tx}} G_{\mathsf{Tx}} G_{\mathsf{Rx}}}{L_{\mathsf{spr}}(f, h) L_{\mathsf{abs}}(f, h, \rho_v)}\right)^{1/2} \tag{23}$$

where $P_{\rm Tx}$ and $G_{\rm Tx}$ are the transmit power and antenna gain, respectively, $G_{\rm Rx}$ is the receiver antenna gain, $L_{\rm spr}=(4\pi hf/c)^2$ are the spreading losses, and $L_{\rm abs}(f,h,\rho_v)$ are the absorption losses, computed as

$$L_{\text{abs}}(f, h, \rho_v) = \exp\left[\int_0^h \kappa(f, h', \rho_v) dh'\right]$$
 (24)

where $\kappa(f,h,\rho_v)$ is the general atmospheric absorption coefficient obtained from the ITU Recommendation ITU-R P.676-12 [56] as well as Recommendation ITU-R P.835 [57]. Notably, the dependence of κ with the temperature and pressure is captured through the dependence with h and the corresponding temperature and pressure profiles, T(h) and P(h), respectively. Fig. 6 depicts the ITU reference atmospheric profiles in [57] used in this study.

TABLE II System Parameters of the Proposed sub-THz DAR ISAC System

Parameter	Value	Parameter	Value
f_1	167 GHz [58]	P_{Tx}	200 mW [58]
f_2	174.8 GHz [58]	G_{Tx}	58 dBi [58]
$T_{ m c}$	1 ms [50]	$G_{ m sat}$	48 dBi [52]
B_{c}	60 MHz [50]	$N_{0,\mathrm{GS}}$	-115 dBm/Hz
H_{sat}	400 km	$N_{0,\mathrm{sat}}$	-135 dBm/Hz

There are two critical assumptions derived from (23) in the sensing CIR: first, the amplitude of the signal reaching a backscattering volume is assumed the same as the corresponding reflection, ignoring the reflectivity of the backscattering volume. Second, the scattering properties of the backscattering range bins are assumed identical at both the online and offline frequencies (or equivalently, that the parameter d described in Appendix A is equal to 1). These two assumptions are reasonable given that DAR estimates the humidity profile solely from the difference in absorbed power at each of the two frequencies, thus not affecting the presented proof of the operational principle of a sub-THz DAR ISAC system. In addition, to verify the system functionalities, we assumed there is signal returns across the entire observed altitude range. In reality, the radar would only capture signal returns from backscattering in the altitude regions where clouds are present.

IV. NUMERICAL RESULTS

The performance analysis of the sub-THz DAR ISAC system through the evaluation procedure outlined above is presented in this section. We first validate the compatibility between DAR and the modulation of the FMCW radar signal in Section IV-A, followed by a study on increasing the data rate and an evaluation of the corresponding sensing performance degradation in Section IV-B. Then, in Section IV-C we provide a detailed analysis of the performance tradeoff between sensing and communication of the proposed DAR-ISAC system. The selected values for the system model variables are included in Table II. We choose a 60 MHz bandwidth, as in Roy et al. [50], to ensure we meet the assumption of constant absorption across the band. Although this is a conservative value for verifying system functionalities, further versions of the system could utilize larger chirp bandwidths while still holding the required assumptions.

For the system parameters utilized, we can evaluate the restrictions in $N_{\rm sc}$ derived in (9) and (10). The latter, which is the less stringent, results in $N_{\rm sc} \ll 3 \times 10^4$, while the former imposes a limitation of $N_{\rm sc} \ll 15,150,1500$ for echoes generated at h=10,1,0.1 km, respectively. For this reason, the values considered are $N_{\rm sc} \in [1,1000]$. Fig. 7 depicts some of the intermediate signals in the system for $N_{\rm sc}=10$, using a 16 QAM modulation, and simulating atmospheric conditions through the "Global Annual" profile.

A. Prioritizing DAR Operation: Impact on Communication

In this section, we compare the humidity estimation profiles obtained using only DAR with those retrieved with a DAR ISAC

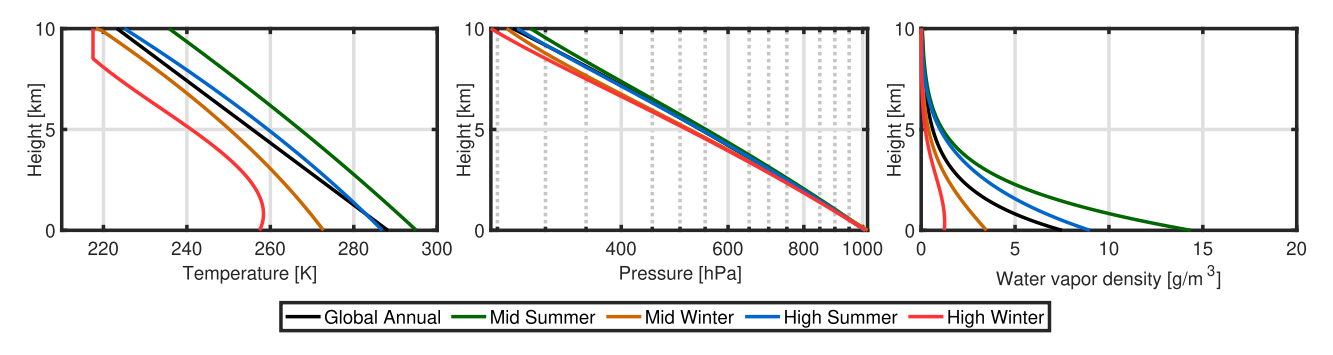


Fig. 6. Temperature, pressure, and humidity profiles from the ITU Recommendation ITU-R P.835 [57] used to test the sub-THz DAR ISAC system.

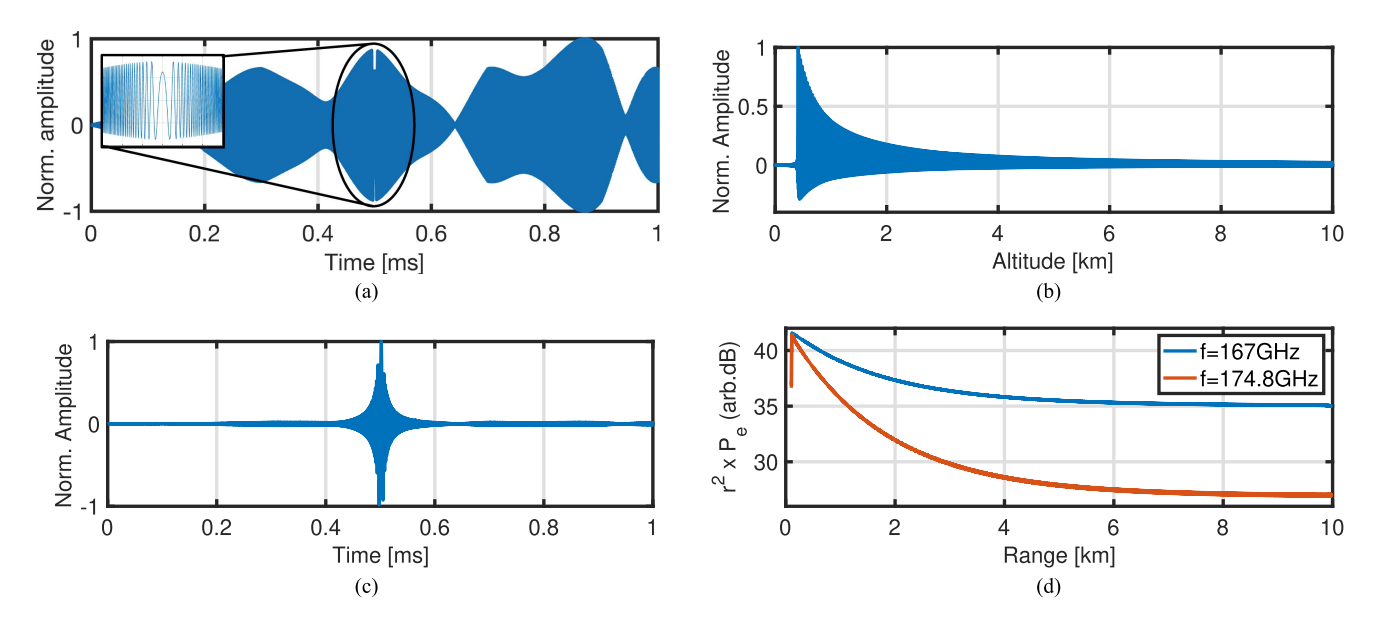


Fig. 7. Intermediate signals in the system model simulation. (a) Real part of one chirp in the baseband transmitted signal s(t). (b) Sensing CIR $\eta_s(t, f_1, \rho_v(h))$. (c) Real part of the received baseband signal $r_s(t, f_1)$. (d) Power-range profiles, $P_e(h, f_i)$, averaging N_c chirps.

waveform with $N_{\rm sc}=1$. Our observations highlight the effectiveness of the DAR ISAC approach while identifying specific areas of estimation error. When conducting sensing exclusively with DAR, the retrieved humidity profiles are identical to those obtained using the DAR ISAC waveform, as observed in Fig. 8. There, we utilized $N_{\rm c}=2000$ chirps per frequency to estimate the humidity profile under "Global Annual" atmospheric conditions. This demonstrates that the integration of communication functionalities does not compromise the accuracy of the DAR-based humidity estimation. The waveforms used for DAR ISAC maintain the integrity of the sensing operation, ensuring reliable humidity profiling when $N_{\rm sc}=1$.

From Fig. 8, we also observe that the first estimated points exhibit a larger estimation error. This discrepancy arises from uncertainty in modeling the radar calibration parameter C(f), as detailed in [58]. Calibration inaccuracies at the initial stages of estimation affect the precision of the humidity profile near the lower altitudes. For this reason, in practice, the radar calibration parameter is estimated by measuring the reflected signal of a target with a well-known radar cross-section, providing more reliable values. In addition, as altitude increases, the estimation

error grows. This trend is attributed to the corresponding decrease in SNR at higher altitudes. The reduced signal strength at greater altitudes impacts the accuracy of the retrieved profiles, leading to larger estimation errors, as indicated by (31).

B. Increasing Data-Rate: Impact on Sensing Accuracy

In this section, we explore the impact of increasing the data rate on the sensing accuracy of the sub-THz DAR ISAC system. There are two primary methods to increase the data rate given a fixed chirp bandwidth $B_{\rm c}$: i) incrementing the number of symbols per chirp, $N_{\rm sc}$, and ii) using higher order modulations. Both approaches have distinct implications in sensing accuracy, and understanding these tradeoffs is crucial for optimizing system performance.

First, we illustrate the impact of increasing $N_{\rm sc}$. Specifically, in Fig. 9 we study the autocorrelation of the transmitted signal, emphasizing the behavior when $N_{\rm sc}>1$. Notably, the autocorrelation curve for $N_{\rm sc}=1$ also represents the autocorrelation of the sensing signal without modulation, underscoring the fact that the ISAC modulation of DAR with $N_{\rm sc}=1$ does not affect

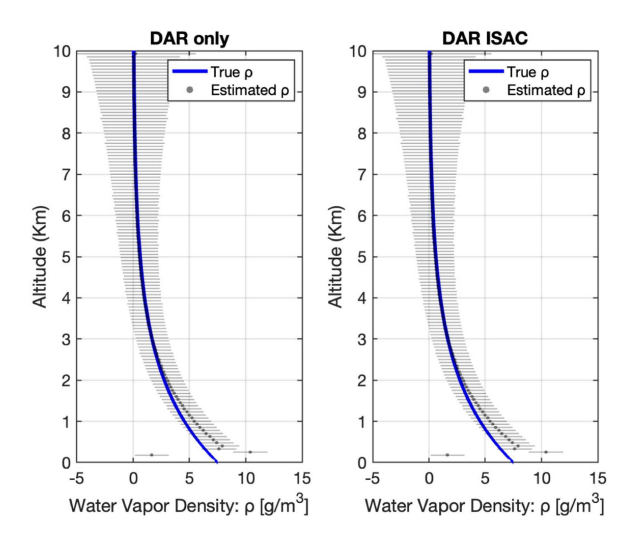


Fig. 8. Retrieved humidity profiles and true profile using DAR, and using a QPSK ISAC modulation with $N_{\rm sc}=1$.

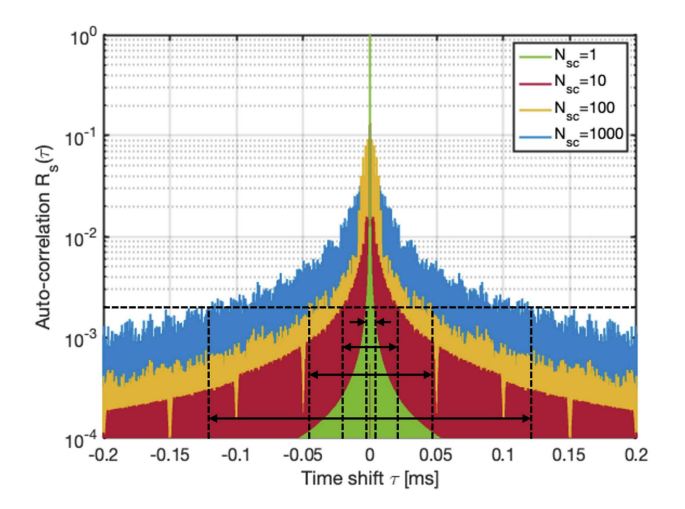


Fig. 9. Rapid degradation of the autocorrelation of s(t) as we increase the data rate through $N_{\rm sc}$.

the performance of the sensing system, as the autocorrelation properties remain unchanged. However, as $N_{\rm sc}$ increases, the signal autocorrelation is significantly degraded. While the autocorrelation still retains a central peak, the side-lobes become larger with increasing $N_{\rm sc}$, indicating an increased interference between adjacent backscattered echoes and, therefore, reduced accuracy in their detection.

This degradation in the autocorrelation properties with $N_{\rm sc}>1$ values is identified as the primary source of degradation in the humidity estimation error when the data rate is increased. The compromised autocorrelation characteristics directly impact the ability of the system to accurately sense and interpret the signal, highlighting the critical tradeoff between data rate and sensing accuracy.

In Fig. 10, we further explore this tradeoff by comparing the humidity retrieval capabilities of the proposed ISAC system under different atmospheric conditions. Each subplot features the true humidity profile represented by a colored line, with the

retrieved humidity profile obtained using the proposed ISAC system depicted by the dark data points with its associated error. Surprisingly, the sensing accuracy for $N_{\rm sc}=10$ and $N_{\rm sc}=100$ (Fig. 10(a) and (b), respectively) remains high across all atmospheric conditions. The retrieved profiles closely match the true humidity profiles, demonstrating the robustness of the ISAC system at these values of $N_{\rm sc}$. However, a significant degradation in humidity estimation is observed when $N_{\rm sc}$ is increased to 1000 [Fig. 10(c)]. This indicates that while the system can handle moderate values of $N_{\rm sc}$ effectively, pushing the data rate too high adversely affects the sensing accuracy.

In addition, a general trend observed across all subplots is that the estimation error grows with altitude, as in Fig. 8. This increase in error is more pronounced under more humid atmospheric conditions, such as those represented by the Summer profiles. In these conditions, the estimation error escalates rapidly with altitude. Conversely, for dry atmospheric conditions like the Winter profiles, the estimation error remains relatively constant, even at higher altitudes. This variability underscores the influence of atmospheric humidity on the performance of the ISAC system, highlighting the need for careful consideration of environmental factors in the design and deployment of such systems.

We summarize the MAE statistics for different values of $N_{\rm sc}$ in Fig. 11. Fig. 11(a) reveals that the estimated values fall close to the diagonal axis, indicating a decent sensing performance for $N_{\rm sc}$ values up to 100, and demonstrating that the estimated humidity values are in good agreement with the true humidity values. However, for $N_{\rm sc}=1000$, the estimated values deviate significantly from the diagonal, highlighting a sharp decline in sensing accuracy and substantial errors in the estimated humidity.

Fig. 11(b) provides an objective perspective of this degradation by depicting the cumulative distribution of the estimation error. From the figure, we observe that the error with a 50% cumulative probability for $N_{\rm sc}=10$ and $N_{\rm sc}=100$ falls within the same order of magnitude as the optimal estimation at $N_{\rm sc}=1$. This emphasizes that moderate increments in $N_{\rm sc}$ do not severely impact sensing accuracy. However, for $N_{\rm sc}=1000$, the estimation error grows by nearly two orders of magnitude. This significant rise in error emphasizes the detrimental impact on sensing accuracy when $N_{\rm sc}$ is excessively increased.

These results highlight the tradeoffs between increasing data rates and maintaining sensing accuracy. While moderate increases in $N_{\rm sc}$ (up to 100) can be managed without severely compromising sensing performance, excessively high values ($N_{\rm sc}=1000$) lead to substantial errors and degraded sensing accuracy. This underscores the importance of optimizing $N_{\rm sc}$ to balance data rate improvements with the need for accurate humidity measurements.

Next, we explore the impact of increasing the data-rate through the modulation order M. As indicated in Section IV, increasing M, does not directly impact the sensing performance of the ISAC system. However, this form of data rate increase has well-known tradeoffs when studying the performance of the communication system. In this regard, we study the BER impact of increasing the system throughput by using higher modulation

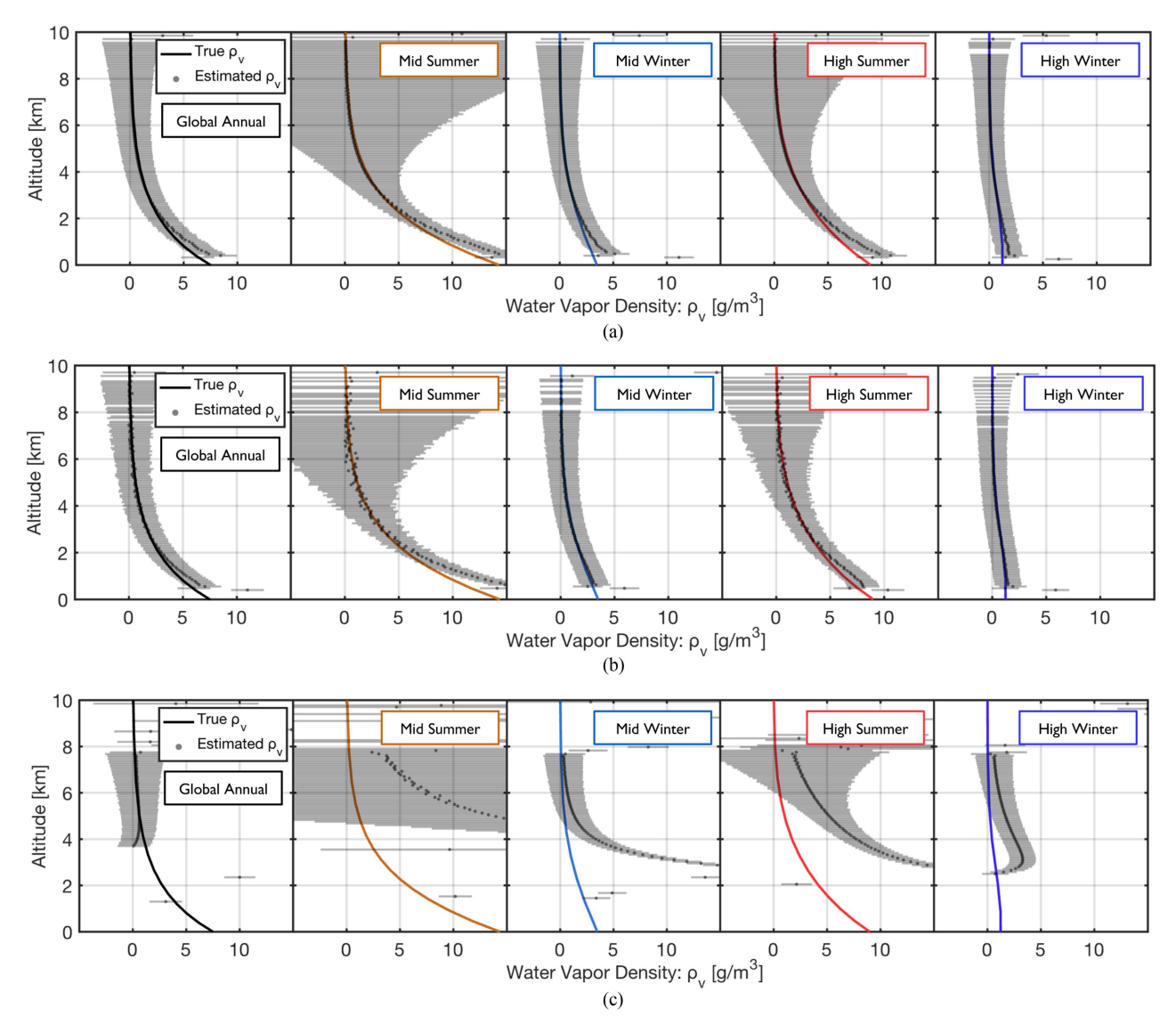


Fig. 10. Comparison of the sub-THz DAR ISAC system humidity retrievals across different atmospheric profiles. Estimated data points are only available where the received SNR is larger than 1 at both frequencies, f_1 and f_2 . (a) Water vapor estimation with $N_{\rm sc}=10$ communication symbols per chirp. (b) Water vapor estimation with $N_{\rm sc}=100$ communication symbols per chirp.

orders, as well as larger $N_{\rm sc}$, in Fig. 12, where we simulated the system performance through the transmission of 10⁴ symbols per frequency. To obtain observable errors without saturating the system memory, we tested high-order QAM modulations, up to M = 1024, plotting them along with theoretical values, indicated by the lines. From the figure, we can clearly observe the effects of the system parameters outlined in (15). Essentially, increasing the modulation order reduces the SNR per bit at a logarithmic scale, while increasing $N_{\rm sc}$ does so linearly. For this reason, focusing on the 16-QAM case for $N_{\rm sc}=10$, if we increase $N_{\rm sc}$ to 100, we observe a $\times 100$ increment in error performance, while if deciding to use a higher order modulation, only a ×36 increment is expected. This emphasizes our observation that, as long as the SNR is large enough, it is better to increase the bit rate by using more spectral efficient modulations, which, in turn, does not affect the sensing performance, as opposed to increasing the number of chirps per symbol.

In Fig. 13, we bring the sensing and communications results together to highlight the performance tradeoff of the proposed sub-THz DAR ISAC system. Concretely, the figure shows the measured MAE and data-rate for each combination of system parameters considered.

From the figure, we observe once more that slightly increasing $N_{\rm sc}$ can significantly enhance the data rate with an unnoticeable increase in MAE. Specifically, for the system values analyzed, increasing $N_{\rm sc}$ up to 100 shows that the data rate can be effectively enlarged up to 500 times while maintaining a minimal impact on sensing accuracy, suggesting that the system can accommodate moderate increases in $N_{\rm sc}$ without compromising performance.

However, a sharp transition in MAE is evident when $N_{\rm sc}=1000$. This indicates a substantial degradation in sensing accuracy, emphasizing that excessively high values of $N_{\rm sc}$ negatively impact the system's ability to accurately estimate the humidity

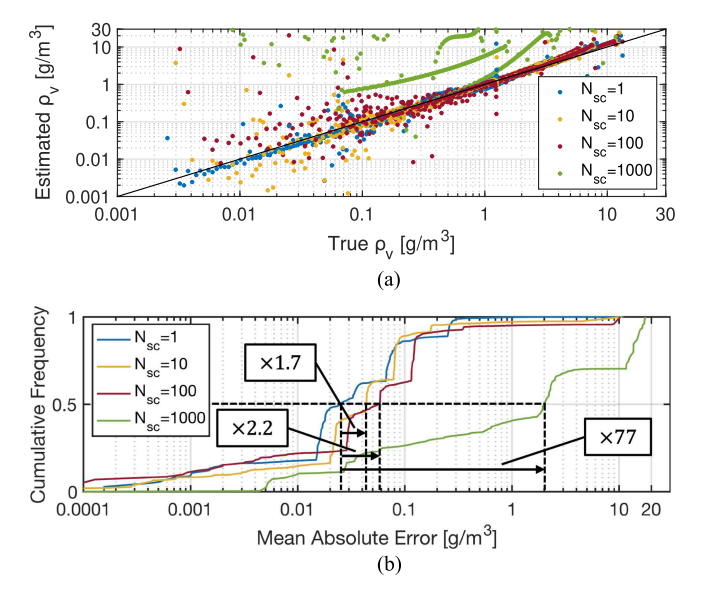


Fig. 11. Summary of MAE statistics for different N_{sc} values. (a) Estimated humidity versus true humidity. (b) Cumulative distribution of the MAE.

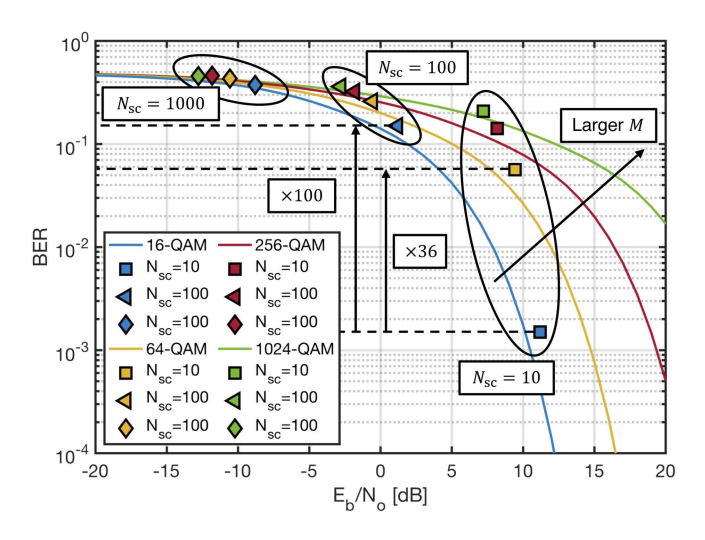


Fig. 12. Communication performance of the sub-THz DAR ISAC system: simulated BER for 10^4 symbols per frequency.

profile, despite the additional data rate increase ($\times 5000$). This highlights the critical tradeoff between data rate and sensing accuracy, where pushing for higher data rates can lead to unacceptable errors in sensing.

Notably, for the case of $N_{\rm sc}=1000$, it is clear that the modulation order appears to have little impact on the MAE, since higher modulation orders do not necessarily result in larger MAE. This further emphasizes that the primary factor affecting sensing accuracy is the increased number of symbols per chirp rather than the modulation scheme itself.

C. Tradeoff Between Sensing and Communications

Based on the previous results, it is clear that the most critical parameter for balancing sensing and communication performance is the number of symbols per chirp N_{sc} . In this section, we provide a detailed analysis of the impact of this parameter as the

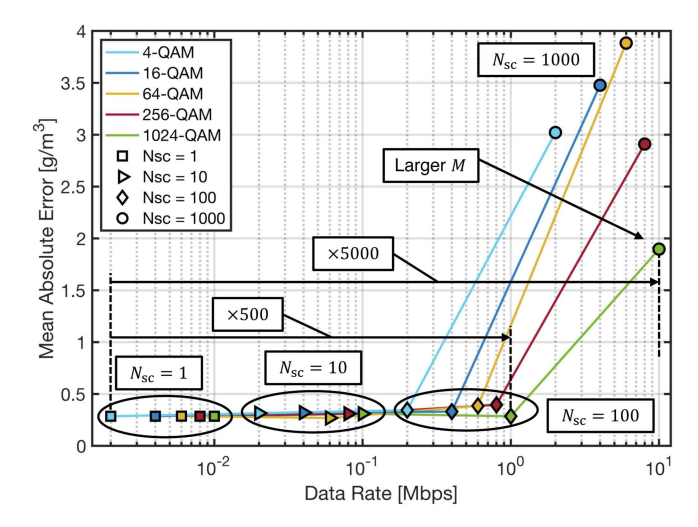


Fig. 13. Communication performance of the sub-THz DAR ISAC system: simulated BER for 10^4 symbols per frequency.

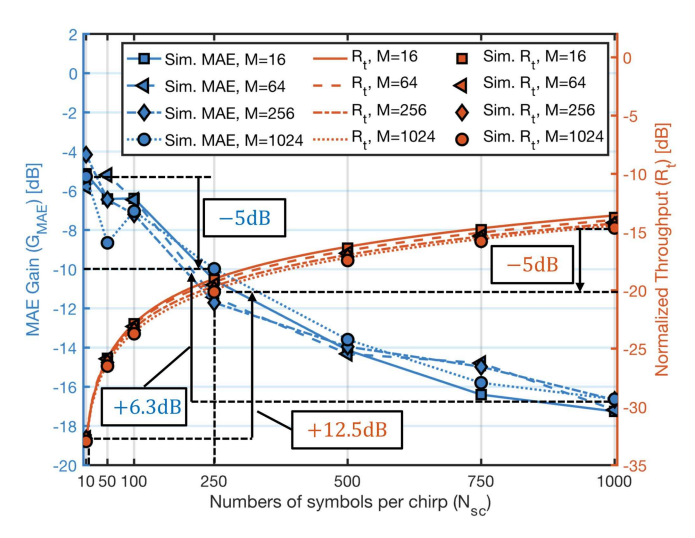


Fig. 14. Analysis of the tradeoff between sensing and communication of the sub-THz DAR-ISAC system.

main driver of the system's performance tradeoff. In Fig. 14, we report the simulated MAE gain on the left axis $G_{\rm MAE}$, as defined in (12), highlighting the degradation in sensing performance when transitioning from a sensing-only system to the proposed ISAC solution. Conversely, on the right axis, we show the simulated throughput over the 10^4 transmitted symbols $R_{\rm t,ISAC}$ normalized by the corresponding throughput of the equivalent communication-only system $R_{\rm t,Comms.}$ given by (19). We also include the theoretical normalized throughput for the continuous range of N_{sc} values between 10 and 1000, as given in (20), further emphasizing the same performance tradeoff between the proposed ISAC system and the equivalent communication-only system.

First, we focus on the throughput. As previously described, the throughput significantly increases with larger values of $N_{\rm sc}$. Notably, the simulated throughput aligns well with the theoretical curves, although it remains slightly below them, likely due to the need for more transmitted bits in practical scenarios. Most remarkably, while the normalized throughput for different

modulation orders appears very similar, it is important to note that the normalized throughput is higher at lower modulation orders. This observation is critical because it indicates that although the absolute data rate is lower at smaller M, and sensing performance remains agnostic to the modulation order, the communication tradeoff of using the proposed ISAC system is less pronounced at these lower M.

Next, we focus on the sensing performance by analyzing the MAE gain. As previously observed, MAE is significantly degraded as $N_{\rm sc}$ increases. Once again, we notice that the MAE is not affected by the modulation order, as the performance remains consistent across different M values, with multiple crossings of the blue curves. If we consider the sensing performance at $N_{\rm sc}=1000$ as unacceptable, then $N_{\rm sc}=250$ appears to be a balanced choice for the proposed DAR-ISAC system. At this value, the sensing accuracy reported is 6.3 dB better, and the communication throughput is about 5 dB lower than at $N_{\rm sc}=1000$. Conversely, the sensing performance is 5 dB worse, while the communication throughput is 12.5 dB higher compared to the case with $N_{\rm sc}=10$.

Despite this appearance of a balanced tradeoff at $N_{\rm sc}=250$, this might not represent the optimal system performance, which depends on the situation and the priority assigned to each capability (remote sensing or communication). The most relevant observation is that, while M does not seem to be a critical parameter and should be kept as high as possible for the available SNR, $N_{\rm sc}$ appears to be the key adjustable parameter when balancing the tradeoff between sensing and communication. As shown in Section II-B, $N_{\rm sc}=1$ yields perfect sensing performance but minimizes throughput. On the other hand, $N_{\rm sc}=1000$ maximizes the throughput of the ISAC system but at the cost of significantly reduced sensing accuracy. Therefore, the value of choice for the appropriate number of symbols modulating each chirp depends on the stakeholder's priorities in the sensing versus communication debate.

V. DISCUSSION

The findings from the previous sections underscore the successful integration of sub-THz communications with DAR in the proposed ISAC system. Our results reveal that the novel DAR-ISAC waveform maintains accurate humidity sensing capabilities even as the communication data rates are increased. This is a significant advancement over previous systems, which did not combine these functionalities.

The key findings from our study are:

- 1) DAR Waveform Compatibility With Communication Modulation: The integration of the DAR waveform with communication modulation is compatible without compromising sensing accuracy, provided that the number of symbols modulating each chirp is limited to one. This result is significant because it demonstrates that high-precision humidity sensing can be maintained while integrating communication capabilities within the same waveform.
- 2) Achieving High Data Rates With Minimal Estimation Error: It was found that data rates can be significantly increased—up to 500 times—without a substantial increase in estimation error by either increasing the modulation order or the number of symbols per chirp. This

- finding suggests that ISAC systems can be optimized to support much higher data throughput without drastically compromising the accuracy of DAR-based sensing.
- 3) Impact of Higher Modulation Orders on Sensing Accuracy: The study also revealed that increasing the data rate through higher modulation orders does not negatively impact sensing accuracy, provided the signal-to-noise ratio (SNR) remains sufficiently high. This indicates that more complex modulation schemes can be employed to enhance data rates in ISAC systems without degrading the quality of the sensing output, making it a preferred approach when high SNR conditions can be ensured.
- 4) Tradeoffs Associated With Increasing the Number of Symbols per Chirp: While increasing the number of symbols per chirp does enhance data rates, this study identified a critical trade-off: beyond a certain threshold (specifically, $N_{\rm sc}=1000$), the estimation error increases due to the degraded auto-correlation properties of the transmitted signal.
- 5) Number of Symbols per Chirp as a Balancing Parameter:
 The number of symbols per chirp emerges as the primary adjustable parameter to balance the tradeoff between sensing accuracy and communication performance. By fine-tuning this parameter, it is possible to optimize ISAC systems for specific operational requirements, whether the priority is higher data rates or more accurate sensing. This finding provides a practical guideline for the design and implementation of ISAC systems in various applications.
- 6) Influence of Atmospheric Humidity on System Performance: The study further reveals that the performance of the ISAC system is sensitive to atmospheric humidity levels. More humid atmospheric profiles lead to greater signal absorption, which degrades sensing accuracy. This suggests that the ISAC system is better suited for operation in drier conditions, where signal absorption is lower, ensuring both high data throughput and accurate sensing.

These findings collectively contribute to the growing body of research on ISAC technologies for remote sensing and set the stage for further exploration of their potential in advanced satellite communication systems.

VI. CONCLUSION

The successful integration of sub-THz communication beyond 100 GHz with DAR, as part of the evolution toward 5G-advanced and beyond 6G NTNs, will enable intrinsic coexistence between both technologies. This integration could potentially lead to the widespread adoption of DAR in current and future satellite constellations, thus enabling ubiquitous in-cloud humidity profiling and climate monitoring. In this direction, this article presents the first study on the performance levels of an ISAC system involving satellite-centric sub-THz communications and DAR.

We propose the adaptation of the DAR waveform to be compatible with communication modulation and mathematically prove its seamless integration without affecting DAR sensing capabilities. Furthermore, we provide two alternatives to increase

the throughput of the communication system with minimal impact on sensing performance: increasing the modulation order and increasing the number of symbols per chirp pulse. All results have been validated by extensive simulation using reference atmospheric models from the ITU and absorption models from the HITRAN database. For the proposed system parameters, we characterized the system tradeoffs in estimation error and communications throughput through extensive simulation.

In conclusion, the findings of this study represent a foundational step toward the development of a comprehensive DAR-ISAC ISAC that integrates precise remote sensing capabilities with high-speed broadband connectivity from space. As advancements in sub-THz and THz hardware continue, the general applicability of the proposed DAR-ISAC system across various frequency bands within the THz and sub-THz spectrum becomes increasingly significant. With numerous additional water vapor absorption peaks within these bands, the proposed system emerges as a robust and future-proof solution, ensuring the seamless coexistence of future broadband sub-THz and THz satellite networks with remote sensing services.

APPENDIX A DAR REGULARIZED LEAST SQUARES APPROACH

We include here a summary of the details to retrieve the estimated water vapor density profile $\hat{\rho}_v(h)$ from the radar power-range profiles $P_e(h,f_i)$ first introduced in [58]. It is assumed that the power-range profiles are discretized to the radar range resolution $\Delta h = c/(2B_{\rm c})$, and only include the values where the reflected power is above the noise floor at both the online and offline frequencies, thus $P_e(h,f_i) \equiv [P_e(h_1,f_i),\ldots,P_e(h_{N_h},f_i)]$, where $h_j=j\Delta h$ for some $j\in\mathbb{N}$, and N_h is the length of the vector of measurements. From here, we compute the corresponding observed reflectivity, $Z_{\rm obs}(h,f_i)=P_e(h,f_i)C(f)h^2$, where C(f) is a calibration coefficient capturing all radar system parameters according to the standard weather radar equation [54]:

$$C(f) = \frac{\lambda^4}{\pi^5 |K_w(f)|^2} \frac{(4\pi)^3}{P_{\text{Tx}} G_{\text{Tx}} \Omega \lambda^2 \Delta h}$$
 (25)

where the dependence of the transmitted power P_{Tx} and antenna gain G_{Tx} with frequency has been omitted, assuming an almost identical hardware response at both online and offline frequencies. λ is the wavelength, Δh is the radar range resolution, Ω is the two-way solid angle, which for a Gaussian beam with a 1/e half beamwidth of θ_0 is equal to $\Omega = \pi \theta_0^2/2$, and $K_w(f) = (\epsilon_w(f) - 1)/(\epsilon_w(f) + 2)$, where $\epsilon_w(f)$ is the complex dielectric constant of liquid water at T = 280 K. We then encode these observations into an observation vector as $\mathbf{y} = [\mathbf{y}_1, \mathbf{y}_2]$ of length $2N_h$, where $[\mathbf{y}_i]_j = \ln(Z_{\mathrm{obs}}(h_j, f_i)/Z_0)$, and $Z_0 = 1 \mathrm{mm}^6/\mathrm{m}^3$. The observed reflectivity is encoded in the logarithmic form to then fit the linear model $\mathbf{y} = F(\mathbf{x}, \mathbf{b}) = \mathbf{K}\mathbf{x} + \mathbf{b}$, where $\mathbf{x} = [\mathbf{x}_1, \mathbf{x}_2]$ are the estimated variables corresponding to $[\mathbf{x}_1]_i = \ln(Z(h_i, f_1)/Z_0)$, and $[\mathbf{x}_2]_i = \rho_v(h_i)$, and \mathbf{K} and \mathbf{b} capture the absorption dependent model parameters.

K is an $2N_h \times 2N_h$ matrix of the form:

$$\begin{bmatrix} \mathbf{I}_{\mathbf{N_h}} & \mathbf{T}(f_1) \\ \mathbf{I}_{N_h} & \mathbf{T}(f_2) \end{bmatrix}$$
 (26)

where \mathbf{I}_{N_h} is the $N_h \times N_h$ identity matrix, and $T(f_i)$ is an $N_h \times N_h$ recursive matrix of the form:

 $\mathbf{T}(f_i)$

$$= \Delta h \begin{bmatrix} \beta_{v}(h_{1}, f_{i}) & 0 & \dots & 0 \\ \beta_{v}(h_{1}, f_{i}) & \beta_{v}(h_{2}, f_{i}) & 0 & 0 \\ \vdots & \vdots & \ddots & \vdots \\ \beta_{v}(h_{1}, f_{i}) & \beta_{v}(h_{2}, f_{i}) & \dots & 0 \\ \beta_{v}(h_{1}, f_{i}) & \beta_{v}(h_{2}, f_{i}) & \dots & \beta_{v}(h_{N_{h}}, f_{i}) \end{bmatrix}$$
(27)

where $\beta_v(h_j, f_i)$ is the water vapor mass extinction cross-section profile, computed as

$$\beta_v(h, f) = \frac{P(h)}{P_0} \frac{T_{\text{STP}}}{T(h)} \frac{N_A}{m_{H_2O}} \sigma_v(f)$$
 (28)

where P(h) and T(h) are the pressure and temperature profiles, known as priors, P_0 and $T_{\rm STP}$ are the standard-pressure-temperature values, N_A is the Avogadro number, m_{H_2O} is the water molar mass, and $\sigma_v(f)$ is the frequency-dependent absorption cross-section of water vapor molecules, computed through the HITRAN line catalog [59]. The bias vector ${\bf b}$ is computed as ${\bf b}=-2[\kappa_d(f_1),\kappa_d(f_2)]+\ln(d)[{\bf 0},{\bf 1}],$ where ${\bf 0}$ and ${\bf 1}$ are vectors of length N_h , d is a scaling factor accounting for different backscattering coefficients between the two frequencies fixed to d=1 in this work for the reasons detailed in Section III-C, and with an uncertainty $\sigma_d=0.1$. $[\kappa_d(f_i)]_j=\kappa_d(h_j,f_i)$, which corresponds to the dry air absorption coefficient profile, computed through the ITU Recommendation ITU-R P.676-12 [56]. The optimization is solved through the regularized least squares approach as

$$\hat{\mathbf{x}} = \left[\mathbf{K}^T (\mathbf{C}_y + \mathbf{C}_e)^{-1} \mathbf{K} + \lambda_{\text{reg}} \mathbf{A} \right]^{-1} \mathbf{K}^T (\mathbf{C}_y + \mathbf{C}_e)^{-1} (\mathbf{y} - \mathbf{b})$$
(29)

and the corresponding retrieved covariance matrix is

$$\hat{\mathbf{C}}_x = \left[\mathbf{K}^T (\mathbf{C}_y + \mathbf{C}_e)^{-1} \mathbf{K} + \lambda_{\text{reg}} \mathbf{A} \right]^{-1}$$
 (30)

where C_y and C_e are the $2N_h \times 2N_h$ covariance matrices capturing the error in the measurement vector y, and the error due to the uncertainty of the parameter d, respectively, and $\lambda_{reg} \geq 0$ is a dimensionless regularization parameter penalizing large humidity gradients in favor of smoother humidity profiles, set to $\lambda_{reg} = 1$. A is block diagonal matrix of the form $\begin{aligned} \mathbf{A} &= \operatorname{diag}(\mathbf{0}_{N_h}, \delta_p^{-2} \mathbf{D}^T \mathbf{\Delta}_h^{-2} \mathbf{D}), \text{ where } \mathbf{0}_{N_h} \text{ is a } N_h \times N_h \text{ null } \\ \operatorname{matrix}, [\mathbf{D}]_{i,j} &= \delta_{i,j-1} - \delta_{i,j} \text{ is a } (N_h - 1) \times (N_h) \text{ finite differ-} \end{aligned}$ encing matrix, where $\delta_{i,j}$ is the Kronecker Delta, and $[\Delta_h]_{i,j}$ $\delta_{i,j}(h_{j+1}-h_j)$ is a $(N_h-1)\times(N_h-1)$ diagonal matrix. The backscattering error covariance matrix is a diagonal matrix of the form $[\mathbf{C}_e]_{i,j} = (\sigma_d/d)^2$ for $i = j, i > N_h$. The measurement error covariance matrix is computed as $\mathbf{C}_y = \mathbf{J}_z \mathbf{C}_z \mathbf{J}_z^T$, where C_z is the observed reflectivity measurement error covariance and J_z is the Jacobinan matrix of the transformation y with respect to $Z_{\text{obs}}(h_j, f_i)$. The covariance matrix C_z is block diagonal of the form $C_z = \text{diag}(C_z(f_1), C_z(f_2))$, where

 $[\mathbf{C}_z(f_i)]_{j,k} = C^2(f_i)h_j^2h_k^2 \text{var}[P_e(h_j, f_i)]\delta_{j,k}$. The variance in the power-range profile measurements is computed through the expression derived in [58] as

$$var[P_e(h, f))] = \frac{P_e(h, f)^2}{N_c} \left(1 + \frac{2}{SNR_s} + \frac{2}{SNR_s^2} \right)$$
 (31)

where $SNR_s = P_e(h, f)/P_{n,s}$ and $P_{n,s}$ are the SNR and noise power at the sensing receiver, respectively.

As discussed, the described retrieval approach estimates the humidity values at altitude ranges of the form $h_j = j\Delta h$ for some $j \in \mathbb{N}$. In practice, the estimated humidity values are retrieved for a coarser set of altitude ranges with resolution $H > \Delta h$, while still using all the N_h measurements at the finer altitude range set $\{h_j\}$. This is done to increase the accuracy of the retrieved profiles given the relatively small difference in absorption cross section at the online and offline frequencies. This change requires some modifications of the forward model $\mathbf{y} = F(\mathbf{K}\mathbf{x} + \mathbf{b})$, involving the projection matrix between the fine altitude range vector set by the radar range resolution and the new oversampled range vector of resolution H. In this work, we used an oversampling factor of O = 30. The details of adjusting the model to incorporate these capabilities are further specified in [58].

REFERENCES

- S. Aliaga, A. J. Alqaraghuli, and J. M. Jornet, "Joint terahertz communication and atmospheric sensing in low earth orbit satellite networks: Physical layer design," in *Proc. IEEE 23rd Int. Symp. World Wireless, Mobile Multimedia Netw.*, 2022, pp. 457–463.
- [2] F. Liu et al., "Integrated sensing and communications: Toward dual-functional wireless networks for 6G and beyond," *IEEE J. Sel. Areas Commun.*, vol. 40, no. 6, pp. 1728–1767, Jun. 2022.
- [3] J. A. Zhang et al., "An overview of signal processing techniques for joint communication and radar sensing," *IEEE J. Sel. Topics Signal Process.*, vol. 15, no. 6, pp. 1295–1315, Nov. 2021.
- [4] J. Keigler, "RCA Satcom: An example of weight optimized satellite design for maximum communications capacity," in *Trends in Communications Satellite*, D. J. Curtin, ed. New York, NY, USA: Pergamon, 1979, pp. 219– 242.
- [5] R. Vicente, G. Nogues, J.-M. Niot, T. Wiertz, P. Contini, and A. Gardelein, "Impacts of laser cooling for low earth orbit observation satellites: An analysis in terms of size, weight and power," *Cryogenics*, vol. 105, 2020, Art. no. 103000.
- [6] Y. Xing and T. S. Rappaport, "Terahertz wireless communications: Cosharing for terrestrial and satellite systems above 100GHz," *IEEE Commun. Lett.*, vol. 25, no. 10, pp. 3156–3160, Oct. 2021.
- [7] "Performance and interference criteria for satellite passive remote sensing," *Int. Telecommunication Union*, vol. RS.2017-0, 2012, Accessed: Oct. 22, 2024. [Online]. Available: https://www.itu.int/rec/R-REC-RS. 2017/en
- [8] S. Millwood, "The orbital internet and the threat to astronomy," in *The Urgent Need for Regulation of Satellite Mega-constellations in Outer Space*, S. Millwood, ed. Berlin, Germany: Springer, 2023, pp. 1–4.
- [9] S. Aliaga, V. Petrov, and J. M. Jornet, "Modeling interference from millimeter wave and terahertz bands cross-links in low earth orbit satellite networks for 6G and beyond," *IEEE J. Sel. Areas Commun.*, vol. 42, no. 5, pp. 1371–1386, May 2024.
- [10] N. Pachler, I. del Portillo, E. F. Crawley, and B. G. Cameron, "An updated comparison of four low earth orbit satellite constellation systems to provide global broadband," in *Proc. IEEE ICC Workshops*, 2021, pp. 1–7.
- [11] R. De Gaudenzi, M. Luise, and L. Sanguinetti, "The open challenge of integrating satellites into (beyond-) 5G cellular networks," *IEEE Netw.*, vol. 36, no. 2, pp. 168–174, Mar./Apr. 2022.
 [12] M. Civas and O. B. Akan, "Terahertz wireless communications in space,"
- [12] M. Civas and O. B. Akan, "Terahertz wireless communications in space," *ITU J. Future Evolving Tech.*, vol. 2, no. 7, pp. 31–38, Oct. 2021.
- [13] W. Jiang et al., "Terahertz communications and sensing for 6G and beyond: A comprehensive review," *IEEE Commun. Surveys Tut.*, to be published, 10.1109/COMST.2024.3385908.

- [14] A. Shafie, N. Yang, C. Han, J. M. Jornet, M. Juntti, and T. Kürner, "Terahertz communications for 6G and beyond wireless networks: Challenges, key advancements, and opportunities," *IEEE Netw.*, vol. 37, no. 3, pp. 162–169, May/Jun. 2023.
- [15] T. S. Rappaport et al., "Wireless communications and applications above 100 GHz: Opportunities and challenges for 6G and beyond," *IEEE Access*, vol. 7, pp. 78729–78757, 2019.
- [16] V. Petrov, T. Kurner, and I. Hosako, "IEEE 802.15.3d: First standardization efforts for sub-terahertz band communications toward 6G," *IEEE Commun. Mag.*, vol. 58, no. 11, pp. 28–33, Nov. 2020.
- [17] I. F. Akyildiz, C. Han, Z. Hu, S. Nie, and J. M. Jornet, "Terahertz band communication: An old problem revisited and research directions for the next decade," *IEEE Trans. Commun.*, vol. 70, no. 6, pp. 4250–4285, Jun. 2022.
- [18] J. V. Siles, K. B. Cooper, C. Lee, R. H. Lin, G. Chattopadhyay, and I. Mehdi, "A new generation of room-temperature frequency-multiplied sources with up to 10× higher output power in the 160-GHz-1.6-THz range," *IEEE Trans. THz Sci. Technol.*, vol. 8, no. 6, pp. 596–604, Nov. 2018.
- [19] Q. Lu, D. Wu, S. Sengupta, S. Slivken, and M. Razeghi, "Room temperature continuous wave, monolithic tunable THz sources based on highly efficient mid-infrared quantum cascade lasers," *Sci. Rep.*, vol. 6, no. 1, Mar. 2016. Art. no. 23595.
- [20] J. V. S. Perez, G. Chattopadhyay, C. Lee, E. T. Schlecht, C. D. Jung-Kubiak, and I. Mehdi, "On-chip power-combining for high-power schottky diode based frequency multipliers," US Patent 9143084B2, Sep. 2015.
- [21] P. Sen, V. Ariyarathna, A. Madanayake, and J. M. Jornet, "A versatile experimental testbed for ultrabroadband communication networks above 100 GHz," *Comput. Netw.*, vol. 193, Jul. 2021, Art. no. 108092.
- [22] P. Sen, J. V. Siles, N. Thawdar, and J. M. Jornet, "Multi-kilometre and multi-gigabit-per-second sub-terahertz communications for wireless backhaul applications," *Nature Electron.*, vol. 6, pp. 1–12, Dec. 2022.
- [23] J. Kokkoniemi, J. M. Jornet, V. Petrov, Y. Koucheryavy, and M. Juntti, "Channel modeling and performance analysis of airplane-satellite terahertz band communications," *IEEE Trans. Veh. Technol.*, vol. 70, no. 3, pp. 2047–2061, Mar. 2021.
- [24] M. Polese et al., "Coexistence and spectrum sharing above 100 GHz," *Proc. IEEE*, vol. 111, no. 8, pp. 928–954, Aug. 2023.
- [25] E. Lansard and J.-L. Palmade, "Satellite constellation design: Searching for global cost-efficiency trade-offs," in *Mission Design & Implementation* of *Satellite Constellations*, J. C. van der Ha, ed. Berlin, Germany: Springer, 1998, pp. 23–31.
- [26] S. Nag, J. LeMoigne, and O. de Weck, "Cost and risk analysis of small satellite constellations for earth observation," in *Proc. IEEE Aerosp. Conf.*, 2014, pp. 1–16.
- [27] C. McGrath, E. Kerr, and M. Macdonald, "An analytical, low-cost deployment strategy for satellite constellations," in *Proc. 13th Reinventing Space Conf.*, S. Hatton, ed. Cham: Springer International Publishing, 2018, pp. 107–116.
- [28] B. H. Cantrell, J. O. Coleman, and G. V. Trunk, "Radar communications," Defense Tech. Inf. Center, vol. 0019, pp. 6–7, Aug. 1981.
- [29] C. Sturm and W. Wiesbeck, "Waveform design and signal processing aspects for fusion of wireless communications and radar sensing," *Proc. IEEE*, vol. 99, no. 7, pp. 1236–1259, Jul. 2011.
- IEEE, vol. 99, no. 7, pp. 1236–1259, Jul. 2011.
 [30] A. M. Elbir, K. V. Mishra, S. Chatzinotas, and M. Bennis, "Terahertz-band integrated sensing and communications: Challenges and opportunities," IEEE Aerosp. Electron. Syst. Mag., 2024, doi: 10.1109/MAES.2024.3476228.
- [31] F. Liu, C. Masouros, A. P. Petropulu, H. Griffiths, and L. Hanzo, "Joint radar and communication design: Applications, state-of-the-art, and the road ahead," *IEEE Trans. Commun.*, vol. 68, no. 6, pp. 3834–3862, Jun. 2020.
- [32] A. Liu et al., "A survey on fundamental limits of integrated sensing and communication," *IEEE Commun. Surveys Tut.*, vol. 24, no. 2, pp. 994–1034, Feb. 2022.
- [33] A. J. Alqaraghuli, J. V. Siles, and J. M. Jornet, "The road to high data rates in space: Terahertz versus optical wireless communication," *IEEE Aerosp. Electron. Syst. Mag.*, vol. 38, no. 6, pp. 4–13, Jun. 2023.
- [34] 3GPP, "Study on new radio (NR) to support non-terrestrial networks," 2020, Accessed: Oct. 22, 2024. [Online]. Available: https://portal.3gpp.org/desktopmodules/Specifications/SpecificationDetails.aspx?specificationId=3234
- [35] Y. Cho, H.-K. Kim, M. Nekovee, and H.-S. Jo, "Coexistence of 5G with satellite services in the millimeter-wave band," *IEEE Access*, vol. 8, pp. 163618–163636, 2020.

- [36] J. Bukhari and W. Mérida, "5G interference with aviation altimeters: Technology and policy recommendations for coexistence," *Transport Policy*, vol. 153, pp. 1–11, Jul. 2024.
- [37] R. Blázquez-García, M. Ummenhofer, D. Cristallini, and D. O'Hagan, "Passive radar architecture based on broadband LEO communication satellite constellations," in *Proc.* 2022 IEEE Radar Conf., 2022, pp. 1–6.
- [38] M. Neinavaie and Z. M. Kassas, "Cognitive sensing and navigation with unknown OFDM signals with application to terrestrial 5G and starlink LEO satellites," *IEEE J. Sel. Areas Commun.*, vol. 42, no. 1, pp. 146–160, Jan. 2024.
- [39] D. Garmatyuk, J. Schuerger, and K. Kauffman, "Multifunctional software-defined radar sensor and data communication system," *IEEE Sensors J.*, vol. 11, no. 1, pp. 99–106, Jan. 2011.
- [40] A. Herschfelt and D. W. Bliss, "Joint radar-communications waveform multiple access and synthetic aperture radar receiver," in *Proc. IEEE 51st Asilomar Conf. Signals, Syst., Comput.*, 2017, pp. 69–74.
- [41] H. Li, J. Xu, C. Sun, S. Wang, X. Wang, and H. Zhang, "Integrated sensing and communication: 3GPP standardization progress," in *Proc.* 2023 21st Int. Symp. Model. Optim. Mobile, Ad Hoc, Wireless Netw., 2023, pp. 1–7.
- [42] A. V. Muppala, A. Alburadi, A. Y. Nashashibi, H. N. Shaman, and K. Sarabandi, "A 223-GHz FMCW imaging radar with 360° FoV and 0.3° azimuthal resolution enabled by a rotationally stable fan-beam reflector," *IEEE Trans. Geosci. Remote Sens.*, vol. 61, 2023, Art. no. 1000709.
- [43] K. B. Cooper et al., "G-band radar for humidity and cloud remote sensing," *IEEE Trans. Geosci. Remote Sens.*, vol. 59, no. 2, pp. 1106–1117, Feb. 2021.
- [44] Z. Lyu et al., "Multi-channel photonic THz-ISAC system based on integrated LFM-QAM WaveForm," J. Lightw. Technol., vol. 42, pp. 1–8, Apr. 2024.
- [45] Y. Liu, O. Li, X. Du, J. Zang, Q. Liu, and G. Wang, "Comprehensive prototype demonstration of ultra-broadband terahertz platform for 6G ISAC," in *Proc. IEEE 34th Annu. Int. Symp. Pers.*, *Indoor Mobile Radio Commun.*, 2023, pp. 1–7.
- [46] A. R. Nehrir et al., "Emerging technologies and synergies for airborne and space-based measurements of water vapor profiles," Surv. Geophys., vol. 38, no. 6, pp. 1445–1482, Nov. 2017.
- [47] K. B. Cooper, "Imaging, Doppler, and spectroscopic radars from 95 to 700 GHz," *Passive Act. Millimeter-Wave Imag. XIX*, vol. 9830, pp. 17–25, May 2016.
- [48] L. Millán, M. Lebsock, N. Livesey, and S. Tanelli, "Differential absorption radar techniques: Water vapor retrievals," *Atmospheric Meas. Techn.*, vol. 9, no. 6, pp. 2633–2646, Jun. 2016.
- [49] K. B. Cooper et al., "Atmospheric humidity sounding using differential absorption radar near 183 GHz," *IEEE Geosci. Remote Sens. Lett.*, vol. 15, no. 2, pp. 163–167, Feb. 2018.
- [50] R. J. Roy et al., "Boundary-layer water vapor profiling using differential absorption radar," *Atmospheric Meas. Techn.*, vol. 11, no. 12, pp. 6511–6523, Dec. 2018.
- [51] R. J. Roy et al., "First airborne measurements with a G-band differential absorption radar," *IEEE Trans. Geosci. Remote Sens.*, vol. 60, 2021, Art. no. 5108115.
- [52] R. J. Roy, M. Lebsock, and M. J. Kurowski, "Spaceborne differential absorption radar water vapor retrieval capabilities in tropical and subtropical boundary layer cloud regimes," *Atmospheric Meas. Techn.*, vol. 14, no. 10, pp. 6443–6468, Oct. 2021.
- [53] Federal Communications Commission (FCC), "FCC Online Table of Frequency Allocations," 2024. Accessed: 2024-06-04. Frequency Range 174.8-191.8 GHz reserved for passive satellite services. [Online]. Available: https://www.fcc.gov/table-frequency-allocations
- [54] M. I. Skolnik, Introduction to Radar Systems, 2nd ed. New York, NY, USA: McGraw-Hill, 1980.
- [55] R. N. McDonough and A. D. Whalen, *Detection of Signals in Noise*. 2nd ed. New York, NY, USA: Academic, 1995.
- [56] International Telecommunication Union, "Attenuation by atmospheric gases and related effects," ITU Radiocommunication Sector, no. P.676-12, 2019, Accessed: Oct. 22, 2024. [Online]. Available: https://www.itu.int/ rec/R-REC-P.676/en
- [57] International Telecommunication Union, "Reference standard atmospheres," ITU Radiocommunication Sector, no. P.676-12, 2017, Accessed: Oct. 22, 2024. [Online]. Available: https://www.itu.int/rec/R-REC-P.835/en
- [58] R. J. Roy, M. Lebsock, L. Millán, and K. B. Cooper, "Validation of a G-band differential absorption cloud radar for humidity remote sensing," *J. Atmospheric Ocean. Technol.*, vol. 37, no. 6, pp. 1085–1102, Jun. 2020.
- [59] L. S. Rothman et al., "The HITRAN 2008 molecular spectroscopic database," J. Quantitative Spectrosc. Radiative Transfer, vol. 110, no. 9, pp. 533–572, Jun. 2009.



Sergi Aliaga Torrens received the two B.Sc. degrees in telecommunications engineering and industrial engineering from the Polytechnic University of Catalonia (UPC), Barcelona, Spain, in 2021. He is currently working toward the Ph.D. degree in the Ultra-broadband Nanonetworking Laboratory (UN-Lab), Institute for the Wireless Internet of Things (WIoT), Northeastern University, Boston, MA, USA.

He was a visiting student in the System Architecture Group at MIT. In 2020, he was awarded a La Caixa fellowship. During his graduate studies, he has

worked as a Researcher at SES Satellite and NASA JPL, received the best paper award in the Second IEEE Workshop on Non-Terrestrial-Networks for 6G, and participated in the 2023 Concurrent Engineering Workshop at the European Space Agency. His research interests include Satellite Communications in the THz band, Signal Processing for Joint Communication and Atmospheric Sensing, Propagation Modelling of THz waves in Space, and Constellation Design for the Next Generation of Non-Terrestrial Networks.



Marco Lanzetti (Graduate Student Member, IEEE) received the Laurea degree in electronic engineering from the University of Pavia, Pavia, Italy, in 2023.

During his studies, he was actively involved in research at the Telecommunication and Remote Sensing Laboratory, University of Pavia. Upon completion of his master's degree, he joined as a visiting student the Ultra-broadband Nanonetworking Laboratory (UNLab), Institute for the Wireless Internet of Things (WIoT), Northeastern University, Boston, MA, USA. His research interests encompass Satellite

Communications in the THz band and Signal Processing techniques for Joint Communication and Atmospheric Sensing.



Vitaly Petrov received the M.Sc. degree in information systems security from SUAI University, St. Petersburg, Russia, in 2011, the M.Sc. degree in IT and communications engineering from Tampere University of Technology, Tampere, Finland, in 2014, and the Ph.D. degree in communications engineering from Tampere University, Finland, in 2020.

He is an Assistant Professor with the Division of Communication Systems, KTH Royal Institute of Technology, Stockholm, Sweden. Before joining KTH in 2024, he was a Principal Research Scientist

with Northeastern University, Boston, MA, USA, from 2022 to 2024; and a Senior Standardization Specialist and a 3GPP RAN1 Delegate with Nokia Bell Labs and later Nokia Standards from 2020 to 2022. He has been a Visiting Researcher with The University of Texas at Austin, Georgia Institute of Technology, and King's College London. His current research interests include short-range and long-range terahertz band communications and networking.

Dr. Petrov was a recipient of the Best Student Paper Award from IEEE VTC-Fall 2015, the Best Student Poster Award from IEEE WCNC 2017, and the Best Student Journal Paper Award from IEEE Finland in 2019.



Anna Vizziello (Senior Member, IEEE) received the Laurea degree in electronic engineering and the Ph.D. degree in electronics and computer science from the University of Pavia, Pavia, Italy, in 2007 and 2011, respectively.

From 2007 to 2009, she was with the European Centre for Training and Research in Earthquake Engineering, Telecommunications and Remote Sensing Group. From 2009 to 2010, she was a Visiting Researcher with the Broadband Wireless Networking Laboratory, Georgia Institute of Technology, Atlanta,

GA, USA, Universitat Politecnica de Catalunya, Barcelona, Spain, in Summer 2009 and Summer 2010, and Northeastern University, Boston, MA, USA, in Winter 2011 and in Summer 2016 and Summer 2023. She is currently an Assistant Professor with the Telecommunications and Remote Sensing Laboratory, University of Pavia, Italy. Her research interests include wireless communications and wearable and implantable sensor systems.

Dr. Vizziello has been included in the 2018 list of "N2Women: Rising Stars in Computer Networking and Communications" for outstanding and impactful contributions in the area of networking/communications, supported by the IEEE Communication Society. She was a co-recipient of the ACM NanoCom'21 Best Paper Award.



Paolo Gamba (Fellow, IEEE) received the Laurea degree (*cum laude*) in electronic engineering and the Ph.D. degree in electronic engineering from the University of Pavia, Pavia, Italy, in 1989 and 1993, respectively.

He is currently a Professor with the Telecommunications and Remote Sensing Laboratory, University of Pavia. He has published more than 200 articles in international peer-reviewed journals.

Dr. Gamba is a fellow of IAPR, AAIA, and the Academia Europaea. He has been invited to give

keynote lectures and tutorials on several occasions about urban remote sensing, data fusion, EO data for physical exposure, and risk management. He was also the Technical Co-Chair for the 2010, 2015, and 2020 IGARSS conferences, Honolulu, Hawaii, USA; Milan, Italy; and online, respectively. He has been elected at the GRSS AdCom from 2014 to 2022. He was the President for IEEE Geoscience and Remote Sensing Society from 2019 to 2020. He is the Editor-in-Chief of IEEE GEOSCIENCE AND REMOTE SENSING MAGAZINE. He was the Editor-in-Chief for IEEE GEOSCIENCE AND REMOTE SENSING LETTERS from 2009 to 2013 and the Chair for the Data Fusion Committee of IEEE GRSS from October 2005 to May 2009.



Josep Miquel Jornet (Fellow, IEEE) received the B.Sc. degree in telecommunication engineering and the Master of Science degree in information and communication technologies from the Universitat Politècnica de Catalunya, Catalunya, Spain, in 2008. He received the Ph.D. degree in electrical and computer engineering from the Georgia Institute of Technology, Atlanta, GA, USA, in 2013.

He is a Professor with the Department of Electrical and Computer Engineering, the Director of the Ultrabroadband Nanonetworking (UN) Laboratory, and an

Associate Director of the Institute for the Wireless Internet of Things (WIoT) at Northeastern University (NU). Between August 2013 and August 2019, he was with the Department of Electrical Engineering at the University at Buffalo (UB), The State University of New York (SUNY). He is a leading expert in terahertz communications, in addition to wireless nano-bio-communication networks and the Internet of Nano-Things. In these areas, he has coauthored more than 240 peer-reviewed scientific publications, including one book, and has been granted five US patents. His work has received over 16 000 citations (h-index of 58 as of December 2023). He is serving as the lead PI on multiple grants from U.S. federal agencies including the National Science Foundation, the Air Force Office of Scientific Research, and the Air Force Research Laboratory as well as industry.

Dr. Jornet is the recipient of multiple awards, including the 2017 IEEE ComSoc Young Professional Best Innovation Award, the 2017 ACM NanoCom Outstanding Milestone Award, the NSF CAREER Award in 2019, the 2022 IEEE ComSoc RCC Early Achievement Award, and the 2022 IEEE Wireless Communications Technical Committee Outstanding Young Researcher Award, among others, as well as six best paper and demo awards. He is a Fellow of the IEEE (Class of 2024) and an IEEE ComSoc Distinguished Lecturer (Class of 2022–2023). He is also the Editor-in-Chief of the Elsevier Nano Communication Networks journal and an Editor for IEEE TRANSACTIONS ON COMMUNICATIONS and Nature Scientific Reports.